
Massive star formation in W51A triggered by cloud-cloud collisions

**Shinji FUJITA^{1,2,3*}, Kazufumi TORII⁴, Nario KUNO^{2,3}, Atsushi
NISHIMURA¹, Tomofumi UMEMOTO^{4,5}, Tetsuhiro MINAMIDANI^{4,5}, Mikito
KOHNO¹, Mitsuyoshi YAMAGISHI⁶, Tomoka TOSAKI⁷, Mitsuhiro
MATSUO⁸, Yuya TSUDA⁹, Rei ENOKIYA¹, Kengo TACHIHARA¹, Akio
OHAMA¹, Hidetoshi SANO¹, Kazuki OKAWA¹, Katsuhiro HAYASHI¹,
Satoshi YOSHIKE¹, Daichi TSUTSUMI¹, Yasuo FUKUI¹ and other FUGIN
members**

¹Department of Astrophysics, Nagoya University, Furo-cho, Chikusa-ku, Nagoya, Aichi, Japan
464-8602

²Department of Physics, Graduate School of Pure and Applied Sciences, University of
Tsukuba, 1-1-1 Tennodai, Tsukuba, Ibaraki, Japan 305-8577

³Tomonaga Center for the History of the Universe, University of Tsukuba, 1-1-1 Tennodai,
Tsukuba, Ibaraki 305-8571, Japan

⁴Nobeyama Radio Observatory, 462-2 Minamimaki, Minamisaku, Nagano, Japan 384-1305

⁵Department of Astronomical Science, School of Physical Science, SOKENDAI (The
Graduate University for Advanced Studies), 2-21-1, Osawa, Mitaka, Tokyo 181-8588, Japan

⁶Institute of Space and Astronautical Science, Japan Aerospace Exploration Agency,
Chuo-ku, Sagami-hara 252-5210, Japan

⁷Department of Geoscience, Joetsu University of Education, Joetsu, Niigata, Japan 943-8512

⁸Graduate Schools of Science and Engineering, Kagoshima University, 1-21-35 Korimoto,
Kagoshima, Kagoshima, Japan 890-0065

Abstract

W51A is one of the most active star-forming regions in the Milky Way, which includes copious amounts of molecular gas with a total mass of $\sim 6 \times 10^5 M_{\odot}$. The molecular gas has multiple velocity components over $\sim 20 \text{ km s}^{-1}$, and interactions between these components have been discussed as the mechanism that triggered the massive star formation in W51A. In this paper, we report an observational study of the molecular gas in W51A using the new ^{12}CO , ^{13}CO , and C^{18}O ($J=1-0$) data covering a $1.^{\circ}4 \times 1.^{\circ}0$ area of W51A obtained with the Nobeyama 45-m telescope at $20''$ resolution. Our CO data resolved four discrete velocity clouds with sizes and masses of $\sim 30 \text{ pc}$ and $1.0-1.9 \times 10^5 M_{\odot}$ around radial velocities of 50, 56, 60, and 68 km s^{-1} . Toward the central part of the HII region complex G49.5-0.4 in W51A, in which the bright stellar clusters IRS 1 and IRS 2 are located, we identified four C^{18}O clumps having sizes of $\sim 1 \text{ pc}$ and column densities of higher than 10^{23} cm^{-2} , which are each embedded within the four velocity clouds. These four clumps are concentrated within a small area of 5 pc, but show a complementary distribution on the sky. In the position-velocity diagram, these clumps are connected with each other by bridge features having weak intensities. The high intensity ratios of ^{13}CO ($J=3-2$)/($J=1-0$) also indicate that these four clouds are associated with the HII regions including IRS 1 and IRS 2. We also revealed that, in the other bright HII region complex G49.4-0.3, the 50, 60, and 68 km s^{-1} clouds show a complementary distribution, with two bridge features connecting between the 50 and 60 km s^{-1} clouds and the 60 and 68 km s^{-1} clouds. An isolated compact HII region G49.57-0.27 located $\sim 15 \text{ pc}$ north of G49.5-0.4 also shows a complementary distribution and a bridge feature. The complementary distribution on the sky and the broad bridge feature in the position-velocity diagram suggest collisional interactions among the four velocity clouds in W51A. The timescales of the collisions can be estimated to be several 0.1 Myrs as crossing times of the collisions, which are consistent with the ages of the HII regions measured from the sizes of the HII regions with the 21 cm continuum data. We discuss a scenario of the cloud-cloud collisions and massive star formation in W51A by comparing these with recent observational and theoretical studies of cloud-cloud collision.

1 Introduction

1.1 W51

Massive stars are influential in the galactic environment by releasing heavy elements and a large amount of energy in ultra-violet (UV) radiation, stellar winds, outflows, and supernova explosions. It is therefore of fundamental importance to understand the mechanisms of massive star formation, and considerable efforts have been made so far (e.g., Wolfire & Cassinelli 1987; Zinnecker & Yorke 2007; Tan et al. 2014). Since giant molecular clouds (GMCs) are the principal sites of massive star formation (e.g., Zinnecker & Yorke 2007), performing large-scale molecular line observations on GMCs at high spatial resolution is important. A spatial resolution less than 1 pc allows one to resolve the dense clumps embedded in GMCs, providing crucial information about massive star formation.

W51 is one of the most active massive star-forming regions in the Milky Way (MW). It was discovered by the observations of the thermal radio continuum emission at 21 cm (Westerhout 1958). The distance to W51 was measured as 5.4 ± 0.3 kpc by Sato et al. (2010) based on the observations of trigonometric parallax, and the total far-infrared luminosity of W51 is as high as $\sim 8 \times 10^6 L_{\odot}$ at 5.4 kpc (Rengarajan et al. 1984). As shown in Figure 1, which shows a two-color composite image of W51 with the *Spitzer* 8 and $24 \mu\text{m}$ data overlaid with the contour map of the 21 cm emission, W51 consists of a number of HII regions for a large area of $\sim 1^{\circ}$, which corresponds to ~ 100 pc at 5.4 kpc, and these HII regions are separated into two major groups, called W51A and W51B, in the northeastern and southwestern parts of W51, respectively (Bieging 1975). The 21 cm radio continuum emission data was taken from THOR (The HI, OH, Recombination line survey of the Milky Way) archive, which is combined with the VGPS data (Beuther et al. 2016; Stil et al. 2006). The total stellar masses included in W51A and W51B were measured as $1.8 \times 10^4 M_{\odot}$ and $1.4 \times 10^4 M_{\odot}$, respectively (Okumura et al. 2000; Kim et al. 2007). A supernova remnant W51C is located in the southeast, which can be traced in the non-thermal radio continuum emission (Koo & Moon 1997a; Koo & Moon 1997b). In this study, we focus on W51A, as it is a young massive star-forming region with ages of a few 0.1–1 Myrs (e.g., Kumar et al. 2004; Ginsburg et al. 2015), providing a unique opportunity to

investigate mechanisms yielding one of the highest star-forming rate in our Galaxy (Okumura et al. 2000).

W51A harbors two bright HII region complexes, GAL 049.5-00.4 and GAL 049.4-00.3 (hereafter called “G49.5-0.4” and “G49.4-0.3”), which each include several HII regions within ~ 10 pc, as shown in the 21 cm continuum emissions in Figure 1(b). In G49.5-0.4, sixteen HII regions, named G49.5-0.4a–i, were identified (Mehringer 1994). The J , H , K' , and $\text{Br}\gamma$ photometric observations by Okumura et al. (2000) identified many O-type and early B-type stars toward these HII regions, as summarized in Table 1. The sizes of these HII regions range from ~ 0.1 pc to ~ 2 pc, and these sizes were used to estimate the ages of these HII regions to be 0.1–2.6 Myr (Okumura et al. 2000). The two outstanding radio sources G49.5-0.4e and G49.5-0.4d are also known as W51 IRS 1 and IRS 2 (Wynn-Williams et al. 1974), which each harbor 4–5 O-type stars and 2–4 early B-type stars, forming bright stellar clusters at the center of G49.5-0.4. The other sources G49.5-0.4a, b, c1, f, h, and i also have multiple O-type/early B-type stars. In addition to these HII regions, many massive young stellar objects (MYSOs) have been identified throughout G49.5-0.4 (Kang et al. 2009; Saral et al. 2017), indicating that massive star formation still continues in this region.

On the other hand, G49.4-0.3 consists of six HII regions G49.4-0.3 a–f with sizes of ~ 0.7 –2 pc (Mehringer 1994). Although there is no photometric identification of the exciting stars of these HII regions, their classifications were estimated to be O4–B0 as listed in Table 1 from the measurements of ionization photons with the 21 cm radio continuum data (Koo 1997). The typical age of the HII regions was measured as ~ 0.2 Myrs (see Section 5.1). Other than G49.5-0.4 and G49.4-0.3, there are several discrete HII regions within ~ 20 pc from G49.5-0.4 or G49.4-0.3, and the classifications of the exciting stars in these sources were measured as O4–B0 from the 21 cm data (see a summary in Table 1).

Molecular gas in W51 shows an extended distribution for ~ 100 pc \times 100 pc, with a total molecular mass measured as $\sim 7.1 \times 10^5 M_{\odot}$ at 5.4 kpc (Carpenter & Sanders 1998). The CO emissions in W51A have multiple velocity components in a radial velocity (line-of-sight velocity) range between ~ 50 –70 km s $^{-1}$. Based on the large-scale ^{12}CO and ^{13}CO ($J=1-0$) observations covering the entirety of the W51 region at an angular resolution of 46'', Carpenter & Sanders (1998) decomposed the velocity structures of molecular gas by performing fits to the CO spectra with multiple Gaussian functions. Subsequently, Okumura et al. (2001) performed ^{13}CO ($J=1-0$) observations at a high angular resolution of 15'' toward a $\sim 15' \times 15'$ area centered on G49.5-0.4. By analyzing the position-velocity diagrams, the authors identified four velocity components around radial velocities of 50, 56, 60, and 68 km s $^{-1}$.

The 68 km s $^{-1}$ cloud corresponds to High Velocity Stream (HVS), which is a filamentary

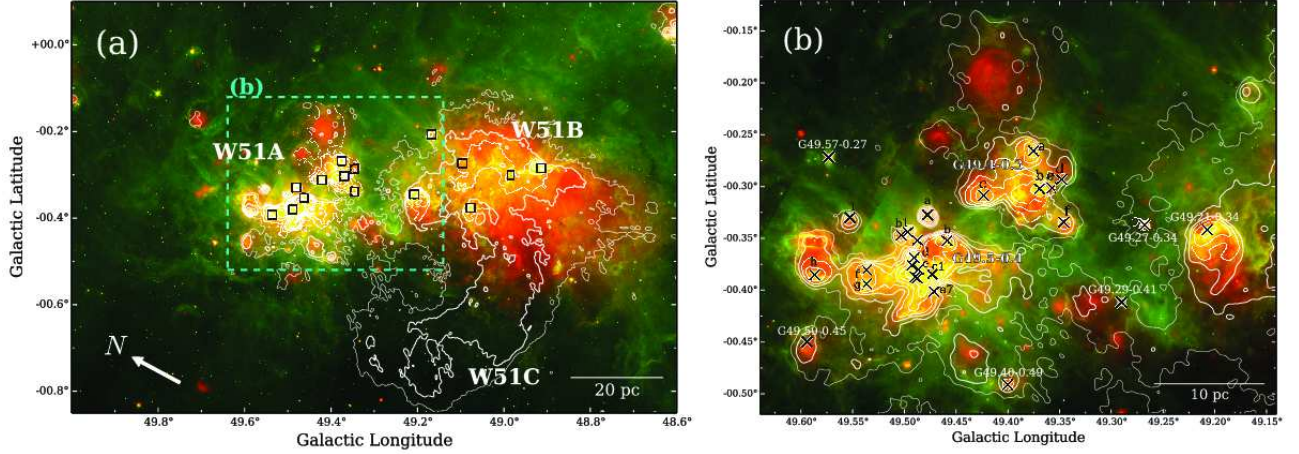


Fig. 1: (a) A composite color image of the *Spitzer*/MIPSGAL 24 μm (red) and *Spitzer*/GLIMPSE 8 μm (green) emissions toward W51. The white contours indicate the THOR 21 cm radio continuum emission combined with the VGPS data (Beuther et al. 2016; Stil et al. 2006), and are plotted from 0.03 (dashed lines) to 3.0 Jy str^{-1} with logarithm step. The angular resolution of the THOR data combined with the VGPS is $25''$. Square symbols represent the compact radio continuum sources identified by Koo (1997). FUGIN data cover the entire region of this map. (b) A close-up view of W51A. The corresponding region is indicated by the box with dashed blue lines in (a). Crosses represent the HII regions listed in Mehringer (1994) (see also Table 1).

molecular cloud stretched nearly parallel to the Galactic plane, overlapping W51A and W51B along the line of sight. The length and width of HVS were measured as ~ 100 pc and ~ 10 pc, respectively (Carpenter & Sanders 1998; Kang et al. 2010; Parsons et al. 2012). Burton & Shane (1970) and Koo (1999) discussed the large velocity of HVS as being attributed to the streaming motion of gas down to the Sagittarius spiral arm driven by the spiral density wave. For the velocity components other than HVS, Carpenter & Sanders (1998) discussed that these represent kinematic structures within a single molecular cloud, the W51 cloud, with a total molecular mass of $\sim 6.0 \times 10^5 M_{\odot}$, referred to as the W51 cloud, whereas Okumura et al. (2001) postulated that these are discrete molecular clouds located at the same distance.

It has been actively debated that the massive star formation in W51A was triggered by collisions between molecular clouds having different radial velocities over $\sim 20 \text{ km s}^{-1}$ (Pankonin et al. 1979; Arnal & Goss 1985; Carpenter & Sanders 1998; Koo 1999; Okumura et al. 2001). Carpenter & Sanders (1998) proposed a collision between the W51 cloud and HVS. The authors revealed that the CO emissions around 60 km s^{-1} in the W51 cloud truncate at the location of HVS, and discussed these two velocity components as being physically related objects at a common distance, suggesting

a collision between these two clouds. Kang et al. (2010) reached the same conclusion, based on the ^{12}CO and ^{13}CO ($J=2-1$) observations at $36''$ resolution, which covered a $1.^\circ25 \times 1.^\circ00$ area of W51. Okumura et al. (2001) argued that a “pileup” scenario of the four discrete molecular clouds resulted in a burst of massive star formation in G49.5-0.4 in W51A.

Recently, supersonic collision between molecular clouds has been discussed as a plausible mechanism of massive star formation. These observational studies of cloud-cloud collisions (CCCs) include the super star clusters and the HII regions in the MW and young O stars in the Large Magellanic Cloud (Fukui et al. 2014; Fukui et al. 2015; Fukui et al. 2017c; Fukui et al. 2018; Furukawa et al. 2009; Hayashi et al. 2017; Kohno et al. 2017; Nishimura et al. 2017a; Nishimura et al. 2017b; Ohama et al. 2010; Ohama et al. 2017a; Ohama et al. 2017b; Sano et al. 2017; Shimoikura et al. 2013; Torii et al. 2011; Torii et al. 2015; Torii et al. 2017a; Torii et al. 2017b; Tsuboi et al. 2015; Takahira et al. 2017; Tsutsumi et al. 2017), where the super star clusters include 10–20 O stars, while the others include a single young O star. Formation of the massive clumps, which may form massive stars, in the collisional-compressed layer was discussed in depth in the magnetohydrodynamical (MHD) simulations by Inoue & Fukui (2013) and Inoue et al. (2017). Kobayashi et al. (2017) formulated the time evolution equation of GMC mass function including CCC, indicating that CCC-driven star formation is mostly driven by massive GMCs having masses $> 10^{5.5} M_\odot$, which may account for a few 10% of the total star formation in the MW and nearby galaxies. Comparisons between the observations and numerical calculations have indicated two important observational signatures of CCCs, i.e., “broad bridge feature” in position-velocity diagrams and “complementary distribution” on the sky between two molecular clouds with different velocities, which provide useful diagnostics to investigate CCCs with molecular line observations (Habe & Ohta 1992; Anathpindika 2010; Takahira et al. 2014; Torii et al. 2017a; Fukui et al. 2018).

1.2 Observational signatures of CCC

Based on comparisons between observations and simulations, Fukui et al. (2018) and Torii et al. (2017a) discussed two possible observational signatures of CCC, i.e., “broad bridge feature” in position-velocity diagrams and “complementary distribution” on the sky between two clouds with different velocities, where the authors assumed a collision between two dissimilar clouds based on the basic CCC scenarios studied by Habe & Ohta (1992), followed by Anathpindika (2010); Takahira et al. (2014); Haworth et al. (2015a); Haworth et al. (2015b); Takahira et al. (2017). A broad bridge feature is relatively weak CO emissions at intermediate velocities between two colliding clouds that

are separated in velocity. When a smaller cloud drives into a larger cloud, a dense compressed layer at the collisional interface is formed, resulting in a thin turbulent layer between the larger cloud and the compressed layer. If one observes a snapshot of this collision with a viewing angle parallel to the colliding axis, two velocity peaks separated by intermediate-velocity emission with lower intensity can be seen in the position-velocity diagrams. The turbulent gas which creates the broad bridge feature can be replenished as long as the collision continues. Several observational studies reported detections of broad bridge features in the CCC regions (e.g., Fukui et al. 2014; Fukui et al. 2016; Fukui et al. 2017a; Furukawa et al. 2009; Ohama et al. 2010; Torii et al. 2015; Torii et al. 2017a).

When two clouds collide, one caves the other owing to the momentum conservation (Haworth et al. 2015b). If the collision takes place head-on between two dissimilar clouds, a cavity will be formed on the larger cloud through this process, and the larger cloud can be seen as a ring-like structure on the sky, unless the observer viewing angle is perfectly perpendicular to the colliding axis. As the size of the cavity corresponds to that of the smaller cloud, the observer with a viewing angle parallel to the colliding axis sees a complementary distribution between the smaller cloud and the ring-like structure of the larger cloud. If the collision is an offset collision, not a head-on collision, the basic process is not changed, and two clouds with different velocities can be observed close to each other. These two clouds may share the boundaries of the clouds on the sky, showing a complementary distribution. Fukui et al. (2017c) and Fukui et al. (2018) pointed out that if the observer viewing angle has an inclination relative to the colliding axis, the complementary distribution has a spatial offset depending on the travel distance of the collision or the depth of the cavity.

In the well-resolved CCC regions, a combination of the two signatures of CCC, broad bridge feature and complementary distribution, may be observed as a “V-shape” gas distribution in the p - v diagram (e.g., Fukui et al. 2018; Ohama et al. 2017b; Hayashi et al. 2017; Torii et al. 2017b). Analyses of the synthetic CO data by Fukui et al. (2018) indicate that, if the observer viewing angle is inclined relative to the colliding axis, the V-shape distribution becomes skewed.

1.3 Paper overview

Following the recent improvement of our knowledge on CCC as a trigger of massive star formation, in this study we present an analysis of the new ^{12}CO , ^{13}CO , and C^{18}O ($J=1-0$) data covering the entirety of W51A in order to test the CCC scenarios as the mechanism of the active massive star formation in W51A. The CO data was obtained using the Nobeyama 45-m telescope at $20''$ resolution, which corresponds to ~ 0.5 pc at 5.4 kpc, as a part of the Galactic plane survey legacy project FUGIN (FOREST Unbiased Galactic plane Imaging survey with the Nobeyama 45-m

telescope) (Minamidani et al. 2016; Umemoto et al. 2017). The advantages of our new CO ($J=1-0$) data can be summarized as follows:

1. We covered a large area of $1.4^\circ \times 1.0^\circ$ including W51A at a comparable spatial resolution with that in the ^{13}CO ($J=1-0$) observations by Okumura et al. (2001), which covered a $\sim 15' \times 15'$ area of G49.5-0.4.
2. Our data includes the C^{18}O ($J=1-0$) emission, which allows us to diagnose the signatures of CCCs in the molecular clouds in W51A. Note that the C^{18}O ($J=1-0$) emission has not been studied for a large area of W51A at such a high angular resolution. Parsons et al. (2012) performed a large-scale ^{12}CO , ^{13}CO , and C^{18}O ($J=3-2$) observations with the James Clerk Maxwell Telescope (JCMT) toward W51A and W51B, providing a comprehensive catalog of the dense gas in the molecular clouds in W51A. However, the authors did not focus on the spatial and velocity distributions of gas with the aim of investigating interactions among different velocity components.
3. Our CO data has a comparable spatial resolution with the JCMT archival CO ($J=3-2$) data (Parsons et al. 2012), allowing us to investigate the excitation conditions of gas, and to probe interaction between molecular gas and HII regions.

In Section 2 we describe the CO dataset used in this study, and in Section 3 we present the main results of the analyses on the CO dataset and comparisons with the other wavelengths. In Section 4 we discuss the results, and present a summary in Section 5.

2 Dataset

The observations of W51A were carried out as a part of FUGIN project (Umemoto et al. 2017) with Nobeyama Radio Observatory (NRO) 45-m telescope. Details of the observations, calibration, and data reduction are summarized in Umemoto et al. (2017), and parameters of the observations and output data are listed in Table 2. In W51A, we covered a $l = 50.0^\circ-48.6^\circ$, $b = -0.9^\circ+0.1^\circ$ ($1.4^\circ \times 1.0^\circ$) in the ^{12}CO ($J=1-0$), ^{13}CO ($J=1-0$), and C^{18}O ($J=1-0$) emissions. A beam size of NRO 45-m telescope is $\sim 15''$ at 115 GHz and an effective angular resolution of this mapping is $\sim 20''$. The SAM45 (Spectral Analysis Machine for the 45-m telescope) spectrometer (Kuno et al. 2011) was used at a frequency resolution of 244.14 kHz, and the effective velocity resolution was 1.3 km s^{-1} at 115 GHz. The typical system noise temperatures including atmosphere were $\sim 150 \text{ K}$ and $\sim 250 \text{ K}$ at 110 GHz and 115 GHz, respectively. The output cube data has spatial grids of $8.5'' \times 8.5''$ and velocity grid of 0.65 km s^{-1} for the ^{12}CO ($J=1-0$), ^{13}CO ($J=1-0$), and C^{18}O ($J=1-0$) emissions. The final root-mean-square (r.m.s) noise temperature T_{rms} in T_{mb} scale are 1.5 K, 0.7 K, and 0.7 K per velocity channel for ^{12}CO ($J=1-0$), ^{13}CO ($J=1-0$), and C^{18}O ($J=1-0$), respectively.

The ^{12}CO ($J=3-2$), ^{13}CO ($J=3-2$), and C^{18}O ($J=3-2$) data were obtained by Parsons et al. (2012) with the Heterodyne Array Receiver Programme (HARP) receiver and the back-end digital autocorrelator spectrometer Auto-Correlation Spectral Imaging System (ACSIS) on the JCMT. The observations covered a $1.^{\circ}4 \times 1.^{\circ}0$ area including W51A and W51B. The data has an angular resolution of $14''$ and a velocity resolution of 0.5 km s^{-1} .

In figures in this paper, to improve a signal-to-noise ratio and compare the FUGIN data with the JCMT data on the same angular resolution, we convolved the dataset with Gaussian of FWHM $22.4''$ and $26.5''$ for the FUGIN data and the JCMT data, respectively (giving the smoothed angular resolutions of $\sqrt{20.0^2 + 22.4^2} \approx 30.''0$ and $\sqrt{14.0^2 + 26.5^2} \approx 30.''0$). We also convolved the dataset for the velocity axis to be a resolution of 1.3 km s^{-1} using the same method.

Table 1: List of the HII regions and massive stars in W51A

Name	Radius (pc)	$\log N_i$ (photons/sec)	Classification	Age (Myr)	Reference
(1)	(2)	(3)	(4)	(5)	(6)
G49.21-0.34	4.9	49.8	[O4]	2.2*	[1]
G49.27-0.34	0.9	45.6	[B0]	1.3*	[1]
G49.29-0.41	–	47.3	[B0]	–	[1]
G49.4-0.3 a	1.6	49.0	[O6]	0.5*	[1, 2]
... b	0.4	49.7	[O5]	0.1*	[1, 2]
... c	1.6	49.3	[O5.5]	0.4*	[1, 2]
... d	1.6	48.6	[O7]	0.6*	[1, 2]
... e	0.3	47.7	[O9.5]	0.1*	[1, 2]
... f	1.6	48.2	[O8.5]	0.8*	[1]
G49.40-0.49	1.3	48.2	[O8.5]	0.5*	[1]
G49.5-0.4 a	1.6	49.0	O5+B1	0.7	[1, 2, 3]
... b	1.6	49.6	O4+O8+B0	2.2	[1, 2, 3]
... b1	0.7	48.2	O9	0.8	[1, 3]
... b2	0.5	47.3	B1	0.2	[1, 3]
... b3	0.5	48.1	[O9]	–	[1]
... c1	–	49.2	O5+O6+B0	0.4	[1, 3]
... d (IRS 2)	1.1	49.7	O4+O6×4+B0+B1×3	0.1	[1, 3]
... e (IRS 1)	0.4	50.4	O4+O5+O6+O8+B0×2	–	[1, 2, 3]
... e1	–	47.9	[O9.5]	–	[1]
... e2	–	>47.6	[>B0]	–	[1]
... e6	–	47.3	[B0]	–	[1]
... e7	–	47.2	B0	0.3	[1, 3]
... f	1.9 (f+g)	49.1	O7+B0+B1×2	1.8	[1, 2, 3]
... g	1.9 (f+g)	48.9	[O5×2+B1]	1.5	[2]
... h	3.2	48.9	O5+B0×4+B1	2.6	[1, 2, 3]
... i	1.6	48.4	O8+B1	1.5	[1, 3]
G49.57-0.27	1.2	47.5	[B0]	0.7*	[1]
G49.59-0.45	3.3	48.7	[O7]	2.1*	[1]

(1) Name of the HII region. (2) Radius of the HII region taken from the web site of the Wide-field Infrared Survey Explorer (WISE) catalog of Galactic HII regions (Anderson et al. 2014; Makai et al. 2017). (3) Ionizing photon flux estimated by Mehringer (1994). (4) Classification of the exciting stars in the HII region estimated by Mehringer (1994) and Okumura et al. (2000). Those derived by measuring ionizing photons from radio continuum image is shown with brackets, while those identified in the near-infrared photometric observations are presented without brackets. (5) Expansion age of the HII region estimated by Okumura et al. (2000) or in this study. Those with asterisk were measured in this study (see Section 4.1). (6) References. [1] Mehringer (1994), [2] Koo (1997), [3] Okumura et al. (2000).

Table 2: Summary of the CO ($J=1-0$) dataset

Observation Date	March – May 2014 and April – May 2015
Observed Area	$l = 50^{\circ}0-48^{\circ}6$, $b = -0^{\circ}9-+0^{\circ}1$ ($1^{\circ}4 \times 1^{\circ}0$)
Telescope	NRO 45-m telescope
Receiver	FOREST
Observation Mode	On-The-Fly
Emission Lines	^{12}CO ($J=1-0$), ^{13}CO ($J=1-0$), and C^{18}O ($J=1-0$)
Angular and Velocity Resolution	$\sim 20''$ (~ 0.5 pc for distance 5.4 kpc) and $\sim 1.3 \text{ km s}^{-1}$
Angular and Velocity Grid of the final cube data	$8.5''$ and 0.65 km s^{-1}
T_{rms}	~ 1.5 K for ^{12}CO ($J=1-0$), ~ 0.7 K for ^{13}CO ($J=1-0$), and ~ 0.7 K for C^{18}O ($J=1-0$)

3 Results

3.1 Large-scale gas distribution

3.1.1 CO ($J=1-0$) distribution

Figures 2(a)–(d) show the integrated intensity maps of the ^{12}CO ($J=1-0$), ^{13}CO ($J=1-0$), C^{18}O ($J=1-0$), and ^{13}CO ($J=3-2$) emissions integrated over $40 - 80 \text{ km s}^{-1}$, which covers the W51A region shown in Figure 1(b). In Figure 2(a) the ^{12}CO ($J=1-0$) emissions show extended gas distributions over the entire map, while the ^{13}CO ($J=1-0$) emissions presented in Figure 2(b) show somewhat clumpy structures. In Figure 2(c) C^{18}O ($J=1-0$) emissions show more clumpy structures than the ^{13}CO ($J=1-0$) emissions. They are strongly detected in G49.5-0.4, indicating the presence of high density gas in this region. The distribution of ^{13}CO ($J=3-2$) emissions (JCMT data obtained by Parsons et al. (2012)) presented in Figure 2(d) resembles that of ^{13}CO ($J=1-0$) emissions, but the intensity is relatively low in the northwestern part of the map.

Figures 3(a)–(d) show the spectra of the ^{12}CO ($J=1-0$), ^{13}CO ($J=1-0$), C^{18}O ($J=1-0$) (FUGIN data), ^{12}CO ($J=3-2$), ^{13}CO ($J=3-2$), and C^{18}O ($J=3-2$) (JCMT data) toward four representative positions. Figure 3(a) shows the spectra at the ^{13}CO ($J=1-0$) peak positions in G49.5-0.4. CO emissions are detected in the velocity range of $45-65 \text{ km s}^{-1}$ and $\sim 68 \text{ km s}^{-1}$ with complicated spectral profiles. Figure 3(b) shows the spectra at the ^{13}CO ($J=1-0$) peak positions in G49.4-0.3. The profiles of the spectra have a peak at $\sim 51 \text{ km s}^{-1}$, while weak CO emissions are detected around $\sim 60 \text{ km s}^{-1}$. The CO emissions at $\sim 68 \text{ km s}^{-1}$ seen toward G49.4-0.3 are barely detected. Figure 3(c) and Figure 3(d) shows the spectra toward the HII region G49.57-0.27 and G49.34-0.21, respectively. CO emissions are detected in several velocity ranges. In addition, in Figure 3(d), we can see that the ^{12}CO ($J=1-0$) and ^{12}CO ($J=3-2$) spectra show self-absorption features at $\sim 66-68 \text{ km s}^{-1}$ indicated by the C^{18}O emissions at the velocity.

Figures 4(a)–(d) show the l - v diagram (integrated along the Galactic latitude over $b = -0^\circ 55 - -0^\circ 10$) and the v - b diagram (integrated along the Galactic longitude over $l = 49^\circ 70 - 49^\circ 10$) of the ^{13}CO ($J=1-0$) emissions and the ^{13}CO ($J=3-2$) emissions. Four discrete velocity components identified in the previous studies (Okumura et al. 2001) can be seen in the spectra, l - v diagram, and v - b diagram, and these clouds are connected with each other by the intermediate velocity emissions. Following the nomenclature by Okumura et al. (2001), we hereafter refer to the velocity components around 50 , 56 , 60 , and 68 km s^{-1} as “the 50 km s^{-1} cloud”, “the 56 km s^{-1} cloud”, “the 60 km s^{-1} cloud”, and “the 68 km s^{-1} cloud (HVS)”, respectively.

Besides these four clouds, we can see a molecular cloud nearby G49.5-0.4 at higher velocity range ($71.6 - 74.8 \text{ km s}^{-1}$) in the velocity channel maps of the ^{12}CO ($J=1-0$) and ^{13}CO ($J=1-0$)

emission (Figure 19 in Appendix 1). It extends perpendicular to the elongation of the 68 km s^{-1} cloud (HVS) down to $b \sim -0.^\circ 5$. Its elongation is perhaps related to feedback of the massive stars in G49.5-0.4. In this paper, we disregard the molecular clouds in this velocity range because their intensity of CO emissions is significantly lower than the other four velocity components.

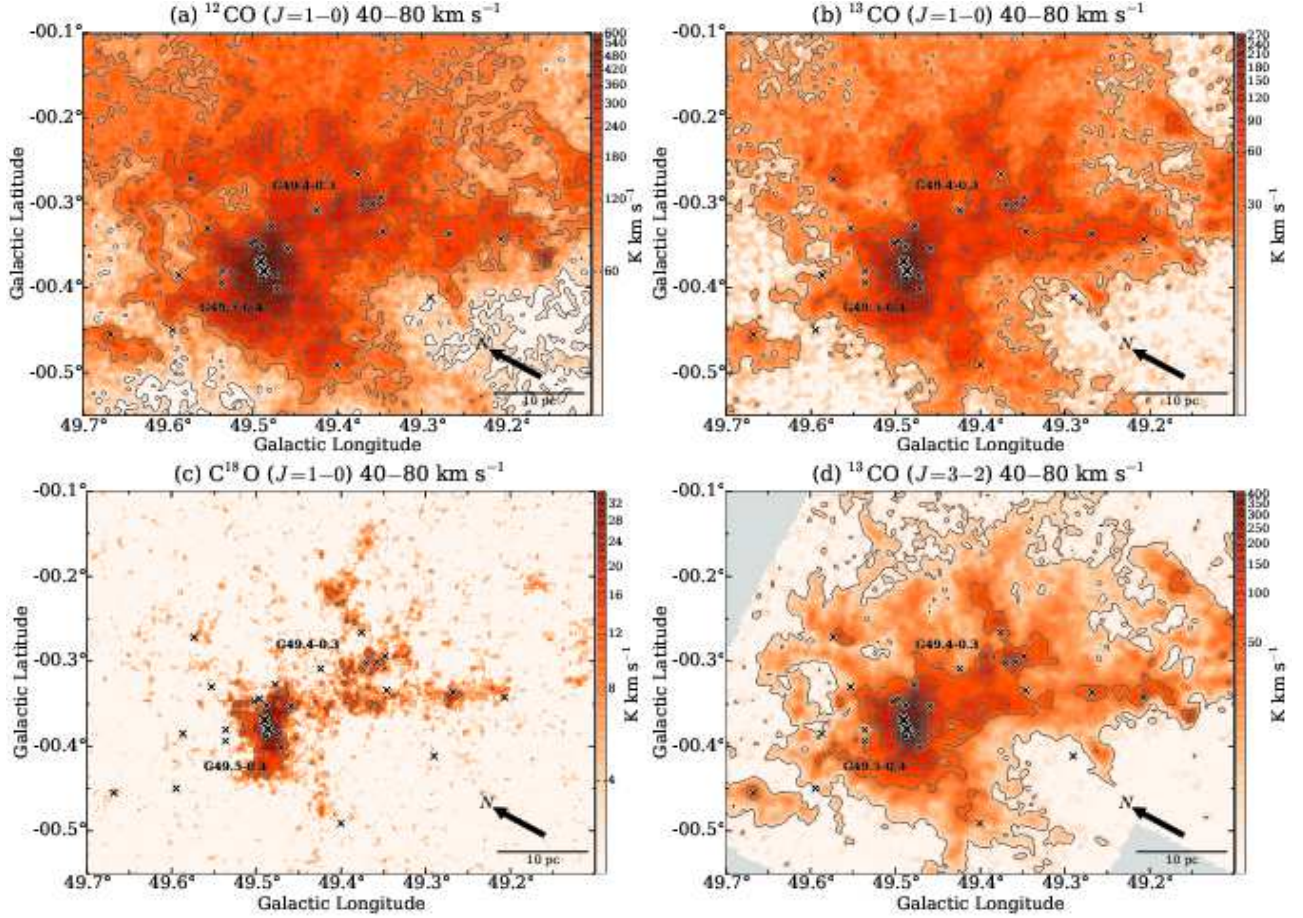


Fig. 2: Integrated intensity map of (a) ^{12}CO ($J=1-0$), (b) ^{13}CO ($J=1-0$), (c) C^{18}O ($J=1-0$), and (d) ^{13}CO ($J=3-2$) integrated over $40-80 \text{ km s}^{-1}$ toward W51A. These maps are colored in logarithmic scale. The contours are plotted with (a) 9σ (60 K km s^{-1}) intervals starting from the 3σ (20 K km s^{-1}) level, (b) 9σ (30 K km s^{-1}) intervals starting from the 3σ (10 K km s^{-1}) level, (c) 3σ (10 K km s^{-1}) intervals starting from the 3σ (10 K km s^{-1}) level, and (d) 2σ (30 K km s^{-1}) intervals starting from the 3σ (50 K km s^{-1}) level, respectively. The gray pixel in (d) indicate the area not covered by JCMT (Parsons et al. 2012).

Figures 5–7 show the ^{12}CO , ^{13}CO and C^{18}O ($J=1-0$) integrated intensity distributions of the four velocity clouds, respectively, overlaid with the contour map of the 21 cm radio continuum data (Stil et al. 2006). We also present the velocity channel maps of the ^{12}CO , ^{13}CO , and C^{18}O emissions in Figure 19 in the appendix for supplements. The ^{12}CO emissions presented in Figure 5 show extended

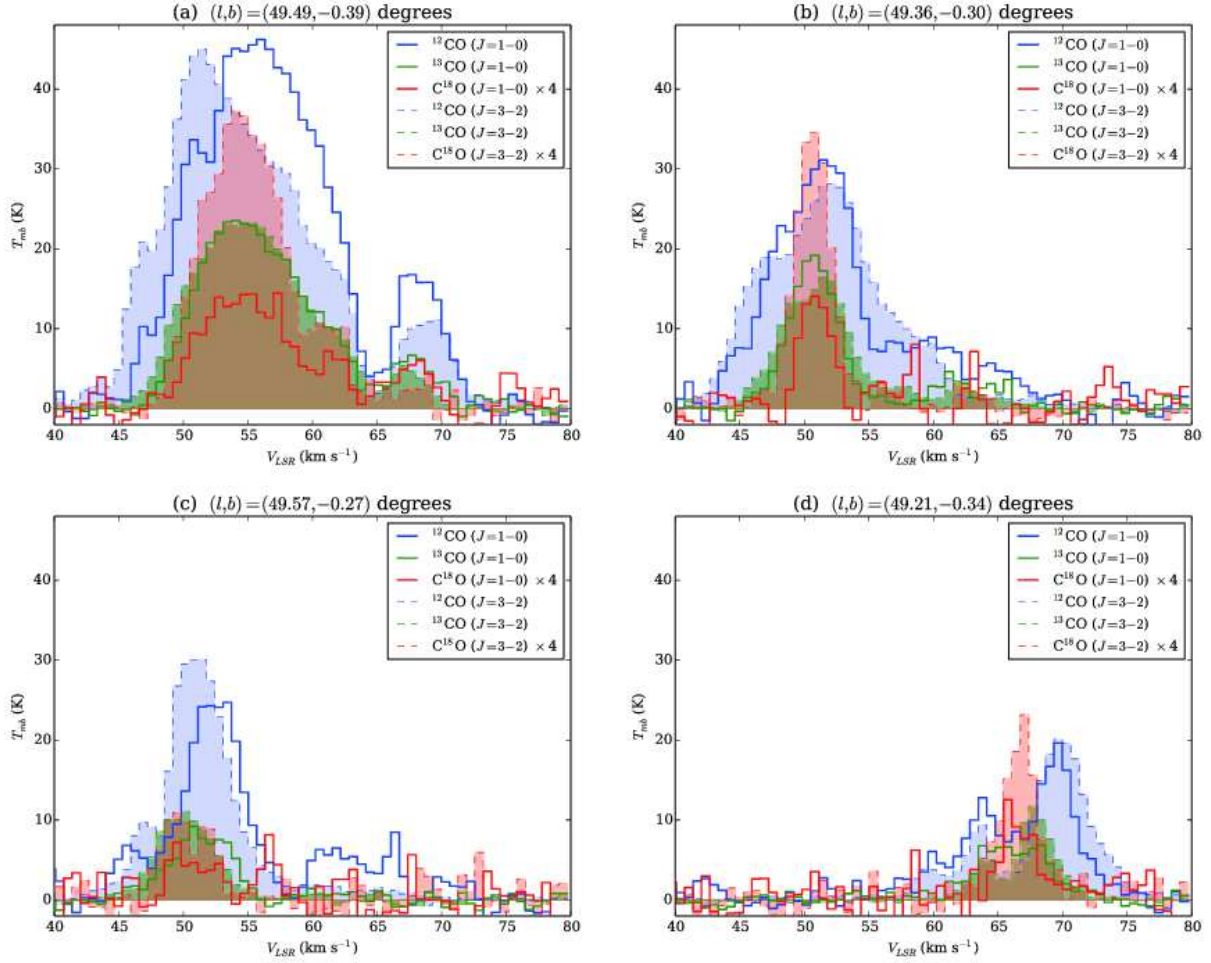


Fig. 3: The CO spectra at (a) $(l, b) = (49^\circ:49, -0^\circ:39)$, (b) $(l, b) = (49^\circ:36, -0^\circ:30)$, (c) $(l, b) = (49^\circ:57, 0^\circ:27)$, and (d) $(l, b) = (49^\circ:21, -0^\circ:34)$. Blue, green, and red lines indicate the profiles of the ^{12}CO , ^{13}CO , and C^{18}O emission lines, respectively. The intensities of the C^{18}O emission lines were multiplied by 4. Solid lines and broken lines (filled) indicate the profiles of the $J=1-0$ and $J=3-2$ emission lines, respectively. The spatial grid size and resolution are $8.''5$ ($= 0''.0023$) and $\sim 30''$ ($= 0''.0083$), respectively.

gas distributions of the four clouds, while the ^{13}CO emissions show that the clouds have networks of clumpy and filamentary structures. C^{18}O probes only clumpy structures except for the 68 km s^{-1} cloud.

The 50 km s^{-1} cloud shown in the panel (a) in Figures 5–7 has strong intensity peaks toward G49.5-0.4 and G49.4-0.3. In the ^{13}CO emissions these peaks are connected with each other with filamentary structures roughly elongated along the northeast-southwest at $b \sim -0^\circ:38$ – $-0^\circ:32$ (Figure 6(a)), which are not apparent in the ^{12}CO emissions (Figure 5(a)), whereas the C^{18}O emissions

show fragmented distributions with sizes of $\sim 2\text{--}3$ pc toward these peaks (Figure 7(a)). We derived the total molecular mass of the 50 km s^{-1} cloud as $\sim 1.1 \times 10^5 M_{\odot}$ using the ^{13}CO ($J=1\text{--}0$) map in Figure 6(a) with an assumption of the local thermodynamic equilibrium (LTE) (e.g., Kawamura et al. 1998). We adopted an abundance ratio $[^{13}\text{CO}]/[\text{H}_2]$ of 1.5×10^{-6} (Dickman 1978), and we estimated excitation temperature T_{ex} for each pixel from the value of the peak brightness temperature of the optically thick ^{12}CO ($J=1\text{--}0$) emissions in the 50 km s^{-1} cloud.

The CO emissions in the 56 km s^{-1} cloud shown in the panel (b) in Figures 5–7 are enhanced at $(l, b) \sim (49^{\circ}48, -0^{\circ}40)$ in G49.5-0.4, whose CO intensities are strongest among the four velocity clouds in W51A. The ^{13}CO emissions show filamentary structures, and some of them are radially elongated from the CO peak at G49.5-0.4 (Figure 6(b)), while the C^{18}O emission is detected only toward the peak with a size of ~ 3 pc (Figure 7(b)). The total molecular mass of the 56 km s^{-1} cloud measured using the ^{13}CO map in Figure 6(b) is $\sim 1.3 \times 10^5 M_{\odot}$.

The 60 km s^{-1} cloud in the panel (c) in Figures 5–7 shows similar gas distribution as the 56 km s^{-1} cloud, as in the ^{13}CO emissions it consists of a strong CO peak at G49.5-0.4, attached with filamentary structures (Figure 6(c)). A difference between the 50 and 56 km s^{-1} clouds is the diffuse ^{13}CO emissions extended above $b \sim -0^{\circ}3$ between l of $49^{\circ}45$ and $49^{\circ}30$. The total molecular mass of the 60 km s^{-1} cloud estimated with the ^{13}CO map is as large as $\sim 1.9 \times 10^5 M_{\odot}$. The C^{18}O distribution in Figure 7(c) is highly fragmented in G49.5-0.4 and G49.4-0.3. Note that the C^{18}O fragments distributed to the east of G49.4-0.3 at $(l, b) \sim (49^{\circ}38, -0^{\circ}32)$ corresponds to a part of the ^{13}CO filamentary structure which surrounds the 21 cm contours of G49.4-0.3 (Figure 6(c)), suggesting possible interaction between the 60 km s^{-1} cloud and G49.4-0.3

In panel (d) in Figures 5–7, the 68 km s^{-1} cloud has a filamentary structure elongated nearly parallel to the galactic plane between l of $49^{\circ}50$ and $49^{\circ}20$. The width of the filament can be measured as $\sim 4\text{--}8$ pc in the ^{12}CO and ^{13}CO emissions, while it is thinner in the C^{18}O emissions, ~ 3 pc. The northeastern tip of the filament is spatially coincident with G49.5-0.4, while the opposite end corresponds to the HII region G49.21-0.34. The total mass of the 68 km s^{-1} cloud is estimated as $\sim 1.3 \times 10^5 M_{\odot}$, which is consistent with the estimate in Carpenter & Sanders (1998).

3.1.2 CO ($J=3\text{--}2/J=1\text{--}0$) intensity ratios

Figures 8(a)–(d) show large-scale distributions of the ^{13}CO ($J=3\text{--}2$)/ ^{13}CO ($J=1\text{--}0$) integrated intensity ratios (hereafter R_{3210}^{13}) of the four clouds in W51A (The associated errors of R_{3210}^{13} is presented in Appendix 2). The four clouds typically have R_{3210}^{13} of higher than 0.6, up to over 2.0, while low R_{3210}^{13} less than 0.2 is seen in the diffuse gas widely distributed at $b > -0^{\circ}30\text{--}0^{\circ}20$ and $b < -0^{\circ}45$. Moreover, to extract the molecular gas heated up by the massive stars in W51A, in Figures 8(e)–(h)

we plot the ^{13}CO ($J=1-0$) contour maps of the four clouds using only the voxels having R_{3210}^{13} of higher than 1.0. In Appendix 3, we performed the large velocity gradient (LVG) analysis, indicating that R_{3210}^{13} of higher than 1.0 can probe the high-temperature gas having > 20 K.

In G49.5-0.4, the high- R_{3210}^{13} gas is seen in all four clouds, and physical associations between these clouds and the HII regions in G49.5-0.4 are thus suggested. In G49.4-0.3, on the other hand, the filamentary structures seen in the $8\ \mu\text{m}$ image are well traced by the high- R_{3210}^{13} gas in the $50\ \text{km s}^{-1}$ cloud, forming an arch-like gas distribution (Figures 8(a) and (e)). The $56\ \text{km s}^{-1}$ cloud is also high in R_{3210}^{13} at the footpoints of the arch-like structure (Figures 8(b) and (f)). In the $60\ \text{km s}^{-1}$ cloud, high- R_{3210}^{13} gas look surrounding the eastern and southeastern rim of the 21 cm emissions of G49.4-0.3 (Figures 8(c) and (g)). The $68\ \text{km s}^{-1}$ cloud show continuous distribution of high- R_{3210}^{13} gas between the east and the south of G49.4-0.3, although its association with G49.4-0.3 is not clear (Figures 8(d) and (h)). These results indicate physical associations of multiple velocity components of gas with G49.5-0.4 and G49.4-0.3.

Associations of the other HII regions with the multiple velocity components can also be investigated in Figures 8(e)–(h). G49.57-0.27 is an isolated HII region situated at the north of G49.5-0.4, which shows high R_{3210}^{13} in the 50 and $56\ \text{km s}^{-1}$ clouds (Figures 8(e) and (f)). There are several relatively expanded HII regions in G49.5-0.4, i.e., G49.5-0.4f, g, h, and i. Although we found no high- R_{3210}^{13} gas spatially overlapping these HII regions, there are several high- R_{3210}^{13} components in the 50 , 56 , and $60\ \text{km s}^{-1}$ clouds which are distributed at the rims of the 21 cm continuum emissions of these HII regions (Figures 8(e)–(g)). As these four HII regions are relatively evolved with ages of an order of 1 Myr as summarized in Table 1, these high- R_{3210}^{13} gas can be interpreted as the remnants of the natal molecular gas of the massive stars in these HII regions. In the other HII regions, we found no plausible signatures of physical association of multiple velocity components. These show either no high- R_{3210}^{13} gas in the four clouds (e.g., G49.29-0.41) or high- R_{3210}^{13} gas only in one cloud (e.g., G49.21-0.34, G49.27-0.34, and G49.59-0.45). In the next subsection, we present the detailed gas distribution toward the individual HII regions which are likely associated with multiple velocity clouds.

3.2 Detailed gas distributions toward individual HII regions

3.2.1 G49.5-0.4

Figure 9 shows a close-up view of G49.5-0.4 with comparisons between the *Spitzer* $8\ \mu\text{m}$ image (Carey et al. 2009) and the C^{18}O contour maps of the four clouds, where the HII regions listed in Table 1 are depicted by crosses, and the MYSOs identified by Saral et al. (2017) are plotted with

triangles. The $8\ \mu\text{m}$ emission is bright around $(l, b) \sim (49^\circ.45\text{--}49^\circ.49, -0^\circ.40\text{--}-0^\circ.33)$, at which many compact HII regions including IRS 1 (G49.5-0.4e) and IRS 2 (G49.5-0.4d) are concentrated. Figure 9 shows that the four clouds have compact and bright C^{18}O emissions within a few pc of the central $8\ \mu\text{m}$ structure.

We identified C^{18}O clumps in this region by drawing a contour at the 70% level of the maximum integrated intensity in the four clouds, resulted in discoveries of the four C^{18}O clumps which are each embedded within the four clouds. Figure 10 shows the C^{18}O ($J=1-0$) spectra at the peak position of each clump. Velocities outside $\pm 5\ \text{km s}^{-1}$ of each peak of the clump are plotted with dashed lines. The physical parameters are summarized in Table 3. The FWHM velocity widths of each spectra are approximately $5\text{--}6\ \text{km s}^{-1}$. The peak column densities of the four clumps in the $50, 56, 60,$ and $68\ \text{km s}^{-1}$ clouds are measured as 2.3, 4.4, 3.9, and $2.7 (\times 10^{23})\ \text{cm}^{-2}$, respectively, from the C^{18}O ($J=1-0$) data by assuming LTE. We here adopted an abundance ratio of $[\text{C}^{18}\text{O}]/[\text{H}_2] = 1.7 \times 10^{-7}$ (Frerking et al. 1982). If we tentatively determine the radii of the clumps as 70% of the peak, virial masses are estimated to be Table 3(8). The LTE masses (Table 3(5)) are almost greater than the virial masses.

Color scale in Figures 11(a), 11(b), and 11(c) show the C^{18}O ($J=1-0$) integrated intensity distributions of the $60\ \text{km s}^{-1}$ cloud, and the blue contours show the C^{18}O ($J=1-0$) integrated intensity distributions of (a) the $50\ \text{km s}^{-1}$ cloud, (b) the $56\ \text{km s}^{-1}$ cloud, and (c) the $68\ \text{km s}^{-1}$ cloud, respectively. In Figure 11(a), the $60\ \text{km s}^{-1}$ cloud surrounds the peak of the $50\ \text{km s}^{-1}$ cloud. In Figure 11(b), the $56\ \text{km s}^{-1}$ cloud and the $60\ \text{km s}^{-1}$ cloud show a complementary distribution. Furthermore, in Figure 11(c), the $60\ \text{km s}^{-1}$ cloud and the $68\ \text{km s}^{-1}$ cloud also show a complementary distribution. The complementary distribution between the 60 and $68\ \text{km s}^{-1}$ clouds was discussed by Carpenter & Sanders (1998) based on their CO observations, and a CCC scenario between these two clouds were suggested by the authors.

Figure 12(a) shows comparisons of the identified four C^{18}O clumps superimposed on the *Spitzer* $8\ \mu\text{m}$ image, where the C^{18}O ($J=1-0$) contours are plotted at 60, 70, 80, and 90 % of the peak intensities of the clumps. Although these four clumps are concentrated within a small area of less than 5 pc, these are not spatially coincident along the line of sight, showing a complementary distribution. Our CO data newly revealed that the complementary distribution are seen not only for the 60 and $68\ \text{km s}^{-1}$ clouds, but also for all four clouds.

The compact HII regions depicted by crosses are distributed around the rims of these four clumps. IRS 2 (G49.5-0.4d) is distributed at the interface of the clumps between the 50 and $60\ \text{km s}^{-1}$ clouds, while IRS 1 (G49.5-0.4e) is seen at the boundaries of the $56, 60,$ and $68\ \text{km s}^{-1}$ clouds. The other HII regions G49.5-0.4e1, e2, and e6 also are distributed at the interface of the four clouds, where

the $8\ \mu\text{m}$ emission is also enhanced (Figure 12(a)). The v - b diagram of the ^{13}CO and C^{18}O ($J=1-0$) emissions shown in Figures 12(b) indicates that the four clumps are connected with each other by the CO emissions with intermediate intensities. These intermediate velocity features are possibly interpreted as the broad bridge features created in the CCC process as discussed in Subsection 1.2. Figure 12(c) shows the v - b diagram of the R_{3210}^{13} . The high R_{3210}^{13} (> 1.5) are seen at the velocity edge and the intermediate velocity of the clouds. In the central molecular zone of the Galaxy, where is a spectacular star-forming environment, Oka et al. (2007) also reported a high CO $J=3-2/J=1-0$ ratio of > 1.5 . The high R_{3210}^{13} in G49.5-0.4 are probably caused by the feedback from the massive stars and/or collisional heating between the clouds.

Table 3: Parameters of the C^{18}O ($J=1-0$) clumps in G49.5-0.4 and G49.4-0.3

cloud name	peak position	C^{18}O ($J=1-0$) W_{max}	R (70%)	M_{LTE} (70%)	$N_{\text{max}}(\text{H}_2)$	FWHM	M_{vir}
	(l, b)	(K km s^{-1})	(pc)	($10^4 M_{\odot}$)	(10^{23} cm^{-2})	(km s^{-1})	($10^4 M_{\odot}$)
(1)	(2)	(3)	(4)	(5)	(6)	(7)	(8)
G49.5-0.4							
50 km s^{-1} cloud	49° 492, -0° 365	11.0	~ 1.1	0.9±0.1	2.3±0.2	4.7±0.2	0.6±0.1
56 km s^{-1} cloud	49° 485, -0° 400	19.7	~ 1.1	2.3±0.1	4.4±0.4	6.3±0.5	1.0±0.2
60 km s^{-1} cloud	49° 495, -0° 379	18.0	~ 0.8	1.0±0.1	3.9±0.4	6.0±0.5	0.7±0.1
68 km s^{-1} cloud	49° 473, -0° 360	12.2	~ 1.0	1.4±0.1	2.7±0.3	6.4±0.7	1.0±0.2
G49.4-0.3							
50 km s^{-1} cloud	49° 360, -0° 303	13.3	~ 0.8	0.3±0.1	2.1±0.2	3.2±0.1	0.2±0.1
56 km s^{-1} cloud	–	–	–	–	–	–	–
60 km s^{-1} cloud	49° 391, -0° 322	8.5	~ 0.9	0.4±0.1	1.8±0.2	4.2±0.5	0.4±0.1
68 km s^{-1} cloud	49° 355, -0° 355	10.2	$\sim 2.5 \times 1.0$	1.6±0.2	2.1±0.2	4.2±0.3	0.7±0.1

(1) Name of the cloud in which the clump is embedded. (2) Peak position of the C^{18}O ($J=1-0$) integrated intensity. (3) Peak integrated intensity the C^{18}O ($J=1-0$). (4) Effective radius of the clump, which was measured at 70% of the peak intensity of the clump. (5) Molecular mass derived from C^{18}O ($J=1-0$) intensity maps assuming LTE within the 70% radius. (6) Maximum H_2 column density of the clump. (7) FWHM of the C^{18}O ($J=1-0$) spectrum at the peak position. These are derived by Gaussian fitting. (8) Virial mass derived from column (4) and (7); $R\Delta v^2/G$, where Δv and G are the FWHM and the gravitational constant, respectively.

3.2.2 G49.4-0.3

Figure 13 shows the ^{13}CO ($J=1-0$) contour maps of the four clouds toward G49.4-0.3. The velocity ranges of the four clouds in each panel are determined from the v - b diagram plotted in Figure 14(b). As already presented in Figure 8, the arch-like CO structure in the 50 km s^{-1} cloud in Figure 13(a) is spatially correlated with the bright $8\ \mu\text{m}$ emissions, which consist of a network of the filamentary structures elongated nearly parallel or perpendicular to the galactic plane. The $8\ \mu\text{m}$ filaments include the HII regions G49.4-0.3a, b, c, d, and e (see Table 1) and MYSOs. G49.4-0.3a, b and e out of them

are spatially coincident with the 50 km s^{-1} cloud, as discussed by Kang et al. (2010).

The 56 km s^{-1} cloud in Figure 13(b) shows diffuse ^{13}CO emissions around the footpoints of the arch-like structure. In addition, there are three CO components, which appear to surround the 21 cm counters of G49.4-0.3, at $(l, b) \sim (49^\circ 32, -0^\circ 25)$, $(49^\circ 33, -0^\circ 36)$, and $(40^\circ 46, -0^\circ 31)$. In Figure 13(c) the filamentary structures of the 60 km s^{-1} cloud shown in Figure 6(c) are plotted. The $8 \mu\text{m}$ filaments stretched nearly parallel to the Galactic plane are traced by the upper rim of the ^{13}CO filamentary structure of the 60 km s^{-1} cloud at $l \sim 49^\circ 34\text{--}49^\circ 43$ and $b \sim -0^\circ 32\text{--}0^\circ 30$. The ^{13}CO filamentary structure harbors high- R_{3210}^{13} gas at the same l range, as shown in Figure 8. The 68 km s^{-1} cloud (HVS) in Figure 13(d) are distributed almost parallel to the filamentary structure in the 60 km s^{-1} cloud.

Figure 14(a) presents the C^{18}O distributions of the four clouds toward G49.4-0.3 in the same manner as in Figure 12(a). While the 56 km s^{-1} cloud is not detected in C^{18}O , the 60 and 68 km s^{-1} clouds show fragmented distribution at $l \sim 49^\circ 34\text{--}49^\circ 40$, and are aligned along the Galactic latitude with the 50 km s^{-1} cloud, showing a complementary distribution. The v - b diagram for this l range is presented in Figure 14(b), which shows that the 60 and 68 km s^{-1} clouds are bridged by the C^{18}O emissions at the intermediate velocities, while the 50 and 60 km s^{-1} clouds are connected with the ^{12}CO emissions at $b \sim -0^\circ 32\text{--}0^\circ 29$ in $55\text{--}60 \text{ km s}^{-1}$, where the spatial distribution of the latter connecting feature is shown in Figure 13(b) in ^{13}CO . These intermediate velocity features may be interpreted as the broad bridge features which suggest interactions between different velocity components. Compared to the $8 \mu\text{m}$ emissions in Figure 14(a), the C^{18}O emissions of the 60 and 68 km s^{-1} clouds correspond to the regions where the $8 \mu\text{m}$ emission is faint. The column density $N(\text{H}_2)$ of the 60 km s^{-1} and 68 km s^{-1} clouds are typically $0.6\text{--}1.0 \times 10^{23} \text{ cm}^{-2}$ (The column density maps are presented in Appendix 4), which corresponds to $A_V \sim 32\text{--}53 \text{ mag}$ (Shetty et al. 2011). Cardelli et al. (1989) and Indebetouw et al. (2005) reported $A_V/A_K \sim 8.8$ ($R_V \sim 3.1$) and $A_{[8.0\mu\text{m}]} / A_K \sim 0.43$, respectively. Therefore, $N(\text{H}_2)$ of $0.6\text{--}1.0 \times 10^{23} \text{ cm}^{-2}$ corresponds $A_{[8.0\mu\text{m}]} \sim 1.5\text{--}2.6 \text{ mag}$. The faintness of the $8 \mu\text{m}$ emission is considered to be an extinction by the 60 km s^{-1} and 68 km s^{-1} clouds, suggesting these two clouds are both located in front of the nebulosities of G49.4-0.3 (Ginsburg et al. 2015), lending further support to the idea that these two clouds are distributed at the same location. At the top of the arch-like structure of the 50 km s^{-1} cloud, where G49.4-0.3a and several MYSOs are distributed, we cannot find complementary distribution among different velocity components, while there is possibly a bridge feature in the ^{13}CO emissions between the 50 and 60 km s^{-1} at $b \sim -0^\circ 24$ (Figure 14(b)).

3.2.3 G49.57-0.27

As presented in Figure 8, G49.57-0.27 shows high R_{3210}^{13} in the 50 and 56 km s⁻¹ clouds. G49.57-0.27 is an isolated compact HII region located at $(l, b) \sim (49.^\circ 57, -0.^\circ 27)$, whose ionizing photon flux measured from a 21 cm continuum map corresponds to a spectral type of B0 (see Table 1). Figure 15(a) shows the ¹³CO ($J=1-0$) integrated intensity maps of the 50 and 56 km s⁻¹ clouds in contours and color, respectively. The CO emission in the 50 km s⁻¹ cloud shows a roughly circular distribution with a diameter of ~ 3 pc, and is spatially coincident with G49.57-0.27 depicted by a cross in Figure 15(a). On the other hand, the 56 km s⁻¹ cloud shows two components separated along the Galactic longitude, and the 50 km s⁻¹ component is sandwiched by these two components, indicating a complementary distribution. In the $l-v$ diagram in Figure 15(b), the 50 km s⁻¹ component is connected with the two separated components in the 56 km s⁻¹ cloud, showing a “V-shape” gas distribution in the ¹²CO ($J=1-0$) emissions. As introduced in Section 2, detections of V-shape gas distribution in the $p-v$ diagram were reported in several CCC regions (e.g., Fukui et al. 2018; Ohama et al. 2017b; Hayashi et al. 2017; Torii et al. 2017b). Based on the synthetic CO observations performed by Haworth et al. (2015a) using the CCC scenarios by Takahira et al. (2014), Fukui et al. (2018) and Torii et al. (2017b) reproduced the V-shape gas distribution in the $p-v$ diagram (see Figure 14 of Fukui et al. (2018)), which resembles the present CO observations shown in Figure 15(a).

4 Discussion

Our analyses of the new CO ($J=1-0$) data basically confirmed the observed features in the previous studies by Carpenter & Sanders (1998) and Okumura et al. (2001). In addition, our CO data including the C¹⁸O ($J=1-0$) emission revealed previously unreported signatures that can be summarized as follows:

1. At the center of G49.5-0.4, in which IRS 1 and IRS 2 are located, the four C¹⁸O clumps, which are each embedded within the four velocity clouds, show a complementary distribution within a small area less than 5 pc (Figure 11). These are connected with each other in the $p-v$ diagram with ¹³CO and/or C¹⁸O emissions (Figure 12), suggesting broad bridge features.
2. In G49.4-0.3, the ¹³CO filamentary structures in the 50, 60, and 68 km s⁻¹ clouds elongated nearly parallel to the Galactic plane are aligned (Figure 6). These filamentary structures show high R_{3210}^{13} near G49.4-0.3 (Figure 8), suggesting physical associations with G49.4-0.3. Each pair of the 50 and 60 km s⁻¹ clouds and the 60 and 68 km s⁻¹ clouds are connected with the bridge features in the $p-v$ diagram (Figure 14).
3. In the relatively evolved HII regions with larger sizes, i.e., G49.5-0.4f, g, h, and i, we found no

CO counterparts which are spatially coincident with the HII regions along the line of sight, but identified the remnant CO fragments in the 50, 56, and 60 km s⁻¹ clouds (e.g., Figure 6), which have high R_{3210}^{13} at the rims of these HII regions (Figure 8).

4. In the isolated HII region G49.57-0.27, a complementary distribution between the gas components in the 50 and 56 km s⁻¹ clouds are discovered (Figure 15), where the circular CO emission in the 50 km s⁻¹ cloud is sandwiched by the two separated components in the 56 km s⁻¹ cloud. The complementary distribution is seen as a V-shape gas distribution in the l - v diagram, which is well reproduced by the numerical calculation of CCC.

In this section, we discuss a CCC scenario in W51A based on the obtained results summarized above.

4.1 Ages of the HII regions

It is important to obtain the ages of the HII regions in W51A in order to discuss the formation mechanism of their exciting stars. Okumura et al. (2000) estimated the ages of the several HII regions listed in Table 1 by measuring sizes of the HII regions. We calculated the ages of the remaining HII regions using the analytical model of the D-type expansion developed by Spitzer (1978), where the sizes of the HII regions and classifications of the exciting sources summarized in Table 1 were adopted. This calculation method is the same as the method Okumura et al. (2000) used. We assumed a uniform initial density of gas as 10⁴ cm⁻³, as the dense gas probed using C¹⁸O is widely detected in the molecular clouds in W51A. The electron temperature was also assumed to be a constant value, 8000 K (e.g., Spitzer 1978). In Table 1 the ages estimated in this study are marked by asterisks. G49.5-0.4 includes HII regions with various ages (0.1–2.6 Myr), while G49.4-0.3 includes only HII regions with ages of <1 Myr.

4.2 CCC scenarios in W51A

There are mainly two CCC scenarios in W51A discussed in the previous studies by Carpenter & Sanders (1998) and Okumura et al. (2001). Carpenter & Sanders (1998) assumed that the present 50, 56 and 60 km s⁻¹ clouds, which correspond to 53, 58, 60, and 63 km s⁻¹ components in Carpenter & Sanders (1998), are inner clouds of a single GMC (the W51 GMC). The authors discovered that the northern tip of the 68 km s⁻¹ cloud is truncated at the location of the 60 km s⁻¹ clouds. Although no detailed process was discussed to create such a complementary distribution, Carpenter & Sanders (1998) postulated a CCC scenario between these the W51 GMC and the 68 km s⁻¹ cloud.

On the other hand, based on the ¹³CO ($J=1-0$) observations in G49.5-0.4, Okumura et al. (2001) discussed CCCs for two pairs of the clouds, i.e., the 56 and 60 km s⁻¹ clouds and the 60 and

68 km s⁻¹ clouds. Although the authors found no plausible evidence of the collision between the 50 and 56 km s⁻¹ clouds, they postulated a CCC scenario that four discrete molecular clouds distributed in a line along the line of sight are moving at different velocities, resulting in the “pileup” of these four clouds.

Our results provide new insight into the CCCs in the W51A region. Figures 11 and 12(a) indicate that the 50, 56, 60, and 68 km s⁻¹ clouds show a complementary distribution. As introduced in Section 1, the recent works on CCC indicate that a complementary distribution can be created through a collision of two molecular clouds of different sizes or with a spatial offset (Torii et al. 2011; Fukui et al. 2018). If so, the present results suggest that multiple collisions of the four clouds have perhaps occurred in G49.5-0.4, resulting in the formation of the massive stars at the interfaces of the collisions. In this scenario, it is reasonably assumed that the observed C¹⁸O clumps were formed through strong compression by the collisions. That the several compact HII regions are concentrated around the interfaces of the complementary distribution lends more credence to this CCC scenario. In Figure 11(a), we could not observe a clear complementary distribution like Figures 11(b) and 11(c).

In G49.5-0.4, the total mass of the dense gas is estimated to be $\sim 5 \times 10^4 M_{\odot}$, and ~ 30 O-stars have been identified (Okumura et al. 2000). If we assume that (1) one O-star was formed in one massive core and (2) the mass of each massive core is $100 M_{\odot}$, which is a value used as an initial mass of the massive core in the simulation of the massive star formation performed by Krumholz et al. (2009), the massive core formation efficiency in the dense gas is estimated to be $\sim 6\%$. This estimation is coarse. To estimate with high accuracy, observational studies with higher spatial resolution are required.

The timescale of the collisions in G49.5-0.4 can be approximately estimated from a ratio of the cloud size and the relative velocity between the two clouds. If we assume the sizes of the four clumps of ~ 2 pc (Table 3) and the relative velocities of 4–18 km s⁻¹, the estimated timescales of the collisions in G49.5-0.4 ranges 0.1–0.5 Myrs. These figures are consistent with the estimated ages of the HII regions distributed around the interfaces of the complementary distribution, which include IRS 1 and IRS 2 (Table 1). While our results indicate that the 50, 56, and 60 km s⁻¹ clouds are almost blended within a small volume, which is consistent with the discussion by Ginsburg et al. (2015) based on the H₂CO absorption observations, spatial correlation of the 68 km s⁻¹ cloud with the extinction in the 8 μ m emission (see Figure 9(d)) shows that it is located in front of G49.5-0.4, not blended with the other three clouds.

In G49.4-0.3, the complementary distribution of gas and presence of the bridge features suggest collisions of the 50 and 60 km s⁻¹ clouds and the 60 and 68 km s⁻¹ clouds (Figure 14). As the filamentary structures in the 60 km s⁻¹ cloud appear to surround the 21 cm continuum emissions of

G49.4-0.3 (Figure 6(c)), it is also possible to interpret the associations of the multiple velocity components in G49.4-0.3 as being to expansion of the HII regions. If so, as the 60 km s^{-1} cloud is redshifted relative to the systemic velocity of the HII regions in G49.4-0.3 having velocities of $\sim 52 \text{ km s}^{-1}$ (Ginsburg et al. 2015), it should be located behind G49.4-0.3. However, as seen in Figure 14(a), the C^{18}O components in the 60 km s^{-1} cloud coincide with the extinction in the $8 \mu\text{m}$ image. This indicates that it is located in front of G49.4-0.3 (Ginsburg et al. 2015), against the assumption of the HII region expansion. On the other hand, in the CCC scenario, the bridge feature in the p - v diagram indicates that the collision is on-going, and it is possible that the 60 km s^{-1} cloud has not completely passed over G49.4-0.3 along the line of sight yet. In the CCC scenario, the dissipative effect of the HII regions still can work on the 60 km s^{-1} cloud to form CO components which surround G49.4-0.3 (indicated by green arrows in Figure 6(c)), suggesting that the 60 km s^{-1} cloud originally had an extended gas distribution in this region.

The timescale of the collision between the 50 and 60 km s^{-1} cloud in G49.4-0.3 can be estimated as 0.2 – 0.6 Myr by assuming collision length ranging from the width of the filamentary structure, ~ 2 pc, to the full extension of the HII regions in G49.4-0.3, ~ 6 pc. On the other hand, as we found no plausible evidence of physical association between the 68 km s^{-1} cloud and the HII regions in G49.4-0.3, it may be that the 60 and 68 km s^{-1} clouds are in the beginning of the collision, and compressed dense gas is observed in C^{18}O as shown in Figure 14(a).

In G49.57-0.27, the V-shape gas distribution in the l - v diagram in Figure 15(b) may also be interpreted by expansion of the HII region. However, as the radius of G49.57-0.27, ~ 1.2 pc (Table 1), is much smaller than that of the 50 km s^{-1} component with 3 – 4 pc, the observed V-shape gas distribution cannot be attributed to expansion of the HII region. It is therefore more likely that the V-shape was formed through the CCC process. If we assume a collision angle relative to the line of sight $\theta = 45^\circ$, the timescale required for the 50 km s^{-1} cloud to completely punch the 56 km s^{-1} cloud can be estimated as 3 – 4 pc / $6 \text{ km s}^{-1} \sim 0.5$ – 0.7 Myr. Although we could not determine an accurate value of θ from position-position-velocity data of molecular clouds, $\theta = 45^\circ$ is one of the convenient solutions as a first approximation of the angle of two colliding clouds (the error of < 5 times is within the range of 86%).

Meanwhile, it is difficult to identify a CCC event in position-position-velocity data when the collision angle is parallel to the sky plane, and thus, there may be unidentified CCCs in W51A. A fraction of such unidentified CCC events with collide angle of $> 80^\circ$ is estimated to be less than 20%, if we tentatively assume that the cloud motions are all random (See Appendix 5). To discuss these unidentified CCC events, we need to conduct statistical study of CCCs in the Galaxy.

4.3 Massive star formation triggered by CCCs in W51A

G49.5-0.4 also includes relatively evolved HII regions with ages of a few Myrs, i.e., G49.5-0.4f, g, h, and i (Table 1). As summarized in the beginning of 4.2, the remnant CO components of these HII regions are found in the 50, 56, and 60 km s⁻¹ clouds. These observed signatures can be interpreted as a CCC scenario or expansion of the HII regions. In the evolved HII regions, complementary distributions and bridge features are dissipated and cannot be observed. Therefore, in G49.5-0.4f, g, h, and i, it is difficult to conclude whether the exciting massive stars in these HII regions were formed via CCCs or not. If we tentatively assume that these HII regions were also formed via the collisions among these three clouds, the collisions should have occurred since a few Myrs ago. The sequential collisions and star formation from the north to the south are consistent with the discussion by Okumura et al. (2001).

In G49.4-0.3, the derived figures in section 4.2 are consistent with the estimated ages of the HII regions (Table 1), implying a scenario that the collision triggered formation of massive stars. In G49.57-0.27, the collision timescale of 0.5–0.7 Myr derived in section 4.2 is also consistent with the estimated age of the HII region of G49.57-0.27, 0.7 Myr (Table 1). As the broad bridge feature indicates that the collision is still continuing, the collision in G49.57-0.27 is likely in the middle, which is consistent with the young age of G49.57-0.27.

Summarizing the discussions in Subsection 4.1–4.2, the observational signatures of CCCs in G49.5-0.4, G49.4-0.3 and G49.57-0.27 represent the collisions which have started since a few 0.1 Myr ago. This indicates that the four velocity components in this region, i.e., the 50, 56, 60, and 68 km s⁻¹ clouds, are currently distributed close to each other, and are partly blended into one single molecular cloud as shown in Figures 16(a) and 16(b), which show the ¹³CO ($J=1-0$) and C¹⁸O ($J=1-0$), respectively, of the four clouds. Besides, Figures 17(c) and 17(d) show the schematic pictures of the ¹³CO ($J=1-0$) distributions in W51A based on Ginsburg et al. (2015) as viewed from the Galactic north pole and the Galactic eastern side, respectively.

This is against for the assumption by Okumura et al. (2001) that the four clouds are located in a line along the line of sight. However, in the latter evolutionary stage of their “pileup” scenario, it can be expected that the four clouds are completely merged into a single cloud (see Figure 5 of Okumura et al. 2001). In this sense, our results are consistent with their CCC scenario.

In Table 4, we compare the properties of the colliding molecular clouds in W51A with those of the other HII regions containing more than 10 O-stars formed by CCC discussed in previous studies. The number of O-stars in G49.5-0.4 and G49.4-0.3 are roughly comparable with those in Westerlund 2, NGC 3603, and RCW 38. Furthermore, the H₂ column density of each the larger cloud is also

roughly comparable ($1 - 3 \times 10^{23} \text{ cm}^{-2}$). However, the molecular mass of the larger cloud in RCW 38 is significantly smaller than that of the other regions. The number of O-stars formed by CCC possibly depend on H_2 column densities rather than molecular masses. The molecular clouds in G49.57-0.27 could not form O-stars because the H_2 column density is low. On the other hand, we can not discuss the relationship between relative line-of-sight velocity separations and the number of O-stars from these data because of a large ambiguity of colliding velocity in 3-dimensional velocity. Figures 18(a)–(c) show the correlations between the number of O-stars and the parameters of the molecular cloud in the HII regions listed in Table 4. As mentioned above, the correlation between the $N_{\text{max}}(\text{H}_2)$ and the number of O-stars (Figure 18(b)) is likely stronger than that of between the molecular mass and the number of O-stars (Figure 18(a)). In addition, there may be a stronger positive correlation also between the number of O-stars and the relative line-of-sight velocity (Figure 18(c)). To establish a quantitative scenario for forming massive stars via a CCC, more studies, such as statistical studies and simulational studies, are required.

Table 4: Physical properties of molecular clouds toward HII regions formed by cloud–cloud collisions

Name	Molecular masses (M_{\odot})	$N_{\text{max}}(\text{H}_2)$ (cm^{-2})	Relative line-of-sight velocities (km s^{-1})	Age (Myr)	Number of O-stars	References
(1)	(2)	(3)	(4)	(5)	(6)	(7)
G49.5-0.4	$\sim 4 \times 10^4$	9×10^{22}	6–20	$\sim 0.1 - 2.6$	28	This study & [1]
...	$\sim 1 \times 10^5$	3×10^{23}				
...	$\sim 1 \times 10^5$	2×10^{23}				
...	$\sim 1 \times 10^5$	7×10^{22}				
G49.4-0.3	$\sim 8 \times 10^4$	1×10^{23}	10	$\sim 0.1 - 0.8$	~ 6	This study & [1]
...	$\sim 9 \times 10^4$	4×10^{22}				
G49.57-0.27	$\sim 1 \times 10^4$	3×10^{22}	6	~ 0.7	0 (one B0-star)	This study & [1]
...	$\sim 4 \times 10^3$	3×10^{22}				
Westerlund 2	9×10^4	2×10^{23}	16	~ 2.0	14	[2], [3]
...	8×10^4	2×10^{22}				
NGC 3603	7×10^4	1×10^{23}	15	~ 2.0	~ 30	[4]
...	1×10^4	1×10^{22}				
RCW 38	2×10^4	1×10^{23}	12	~ 0.1	~ 20	[5]
...	3×10^3	1×10^{22}				

(1) Name of HII regions. (2) Molecular mass derived from the ^{12}CO ($J=1-0$) and ^{13}CO ($J=1-0$) data by assuming LTE. (3) Maximum H_2 column density derived from the ^{12}CO ($J=1-0$) and ^{13}CO ($J=1-0$) data by assuming LTE. (4) Relative line-of-sight velocity separation among the colliding clouds. (5) Age of HII regions. (6) Number of O-stars. (7) References. [1] Okumura et al. (2000), [2] Furukawa et al. (2009), [3] Ohama et al. (2010), [4] Fukui et al. (2014), and [5] Fukui et al. (2016).

5 Summary

We carried out new ^{12}CO ($J=1-0$), ^{13}CO ($J=1-0$), and C^{18}O ($J=1-0$) observations toward W51A as a part of the FUGIN project with the Nobeyama 45-m telescope. These observations covered a large area of W51A ($1.4^\circ \times 1.0^\circ$) at an angular resolution of $20''$ (~ 0.5 pc). The main conclusions of the present study are summarized as follows:

1. Our CO data identified four discrete velocity clouds with sizes and masses of ~ 30 pc and $1.0-1.9 \times 10^5 M_\odot$ at radial velocities of 50, 56, 60, and 68 km s^{-1} in W51A. These four clouds mainly consist of the bright CO emissions toward the two bright HII region complexes G49.5-0.4 and G49.4-0.3 attached with the filament hub structures elongated for several tens pc.
2. Based on comparisons between our ^{13}CO ($J=1-0$) data and the archival the JCMT ^{13}CO ($J=3-2$) data, it was revealed that all of these four clouds are physically associated with G49.5-0.4, while three of the four, i.e., 50, 60, and 68 km s^{-1} clouds, are interact with G49.4-0.3, as the ^{13}CO ($J=3-2$)/ ^{13}CO ($J=1-0$) intensity ratios in these clouds are increased higher than 1.0 near the HII regions. The LVG calculations indicate such high ratios can be attributed to high temperature gas heated by the massive stars in these regions. We also found that the isolated HII region G49.57-0.27 located ~ 15 pc north of G49.5-0.4 are associated with the 50 and 56 km s^{-1} clouds.
3. In each of these three HII regions G49.4-0.5, G49.4-0.3, and G49.25-0.27, we revealed that the multiple velocity components associated with the HII regions show “spatially complementary distributions” on the sky and “broad bridge features” in the position-velocity diagrams. In particular, in G49.25-0.27 a combination of the complementary distribution and the bridge features represent a “V-shape” gas distribution in the position-velocity diagram. These signatures have been discussed as the observational signatures of CCC in recent theoretical and observational studies in the galactic HII regions.
4. We estimated the timescales of the collisions in these three regions to be several 0.1 Myrs by calculating crossing times of the collisions. These estimates are consistent with the ages of the HII regions measured from the sizes of the HII regions with the 21 cm continuum map.
5. Our present results lend more credence to the CCC scenario in W51A, that multiple velocity components have been continuously colliding with each others, resulting in active massive star formation in W51A.
6. On the other hand, our results are also consistent with the discussion by Carpenter & Sanders (1998) that the 50, 56, and 60 km s^{-1} clouds represent kinematic structure within a single molecular cloud, as the total molecular mass in W51 is consistent with its virial mass for 100 pc scale, suggesting that self-gravity will play a critical role in the evolution of the molecular clouds in

W51. To fully understand the kinematics and interactions of molecular clouds in W51, which will allow us to investigate the future of this region, it is important to study W51B using the same CO dataset. We will work on this issue in a separate paper.

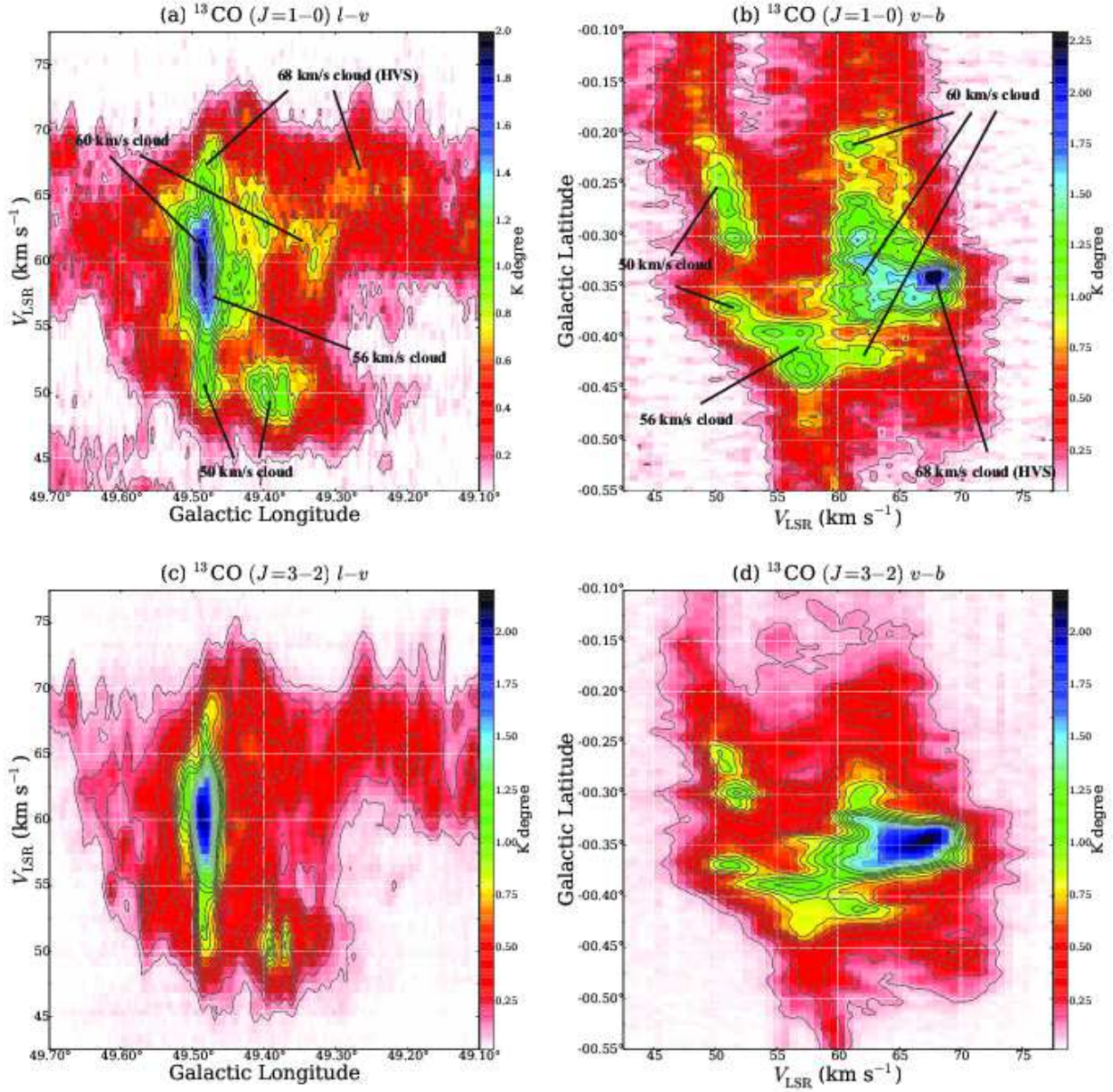


Fig. 4: (a) The Galactic Latitude–Velocity ($l-v$) diagram of the ^{13}CO ($J=1-0$) emissions integrated over $b = -0^\circ.55 - -0^\circ.10$. The contours are plotted with 5σ (0.11 K degrees) intervals starting from the 5σ (0.11 K degrees) level. (b) The Velocity–Galactic Latitude ($v-b$) diagram of the ^{13}CO ($J=1-0$) emissions integrated over $l = 49^\circ.70 - 49^\circ.10$. The contours are plotted with 5σ (0.13 K degrees) intervals starting from the 5σ (0.13 K degrees) level. (c) Same as (a), but for the ^{13}CO ($J=3-2$) emissions. The contours are plotted at every 5σ (0.09 K degrees) from 0.09 K degrees ($\sim 5\sigma$). (d) Same as (b), but for the ^{13}CO ($J=3-2$) emissions. The contours are plotted with 5σ (0.11 K degrees) intervals starting from the 5σ (0.11 K degrees) level.

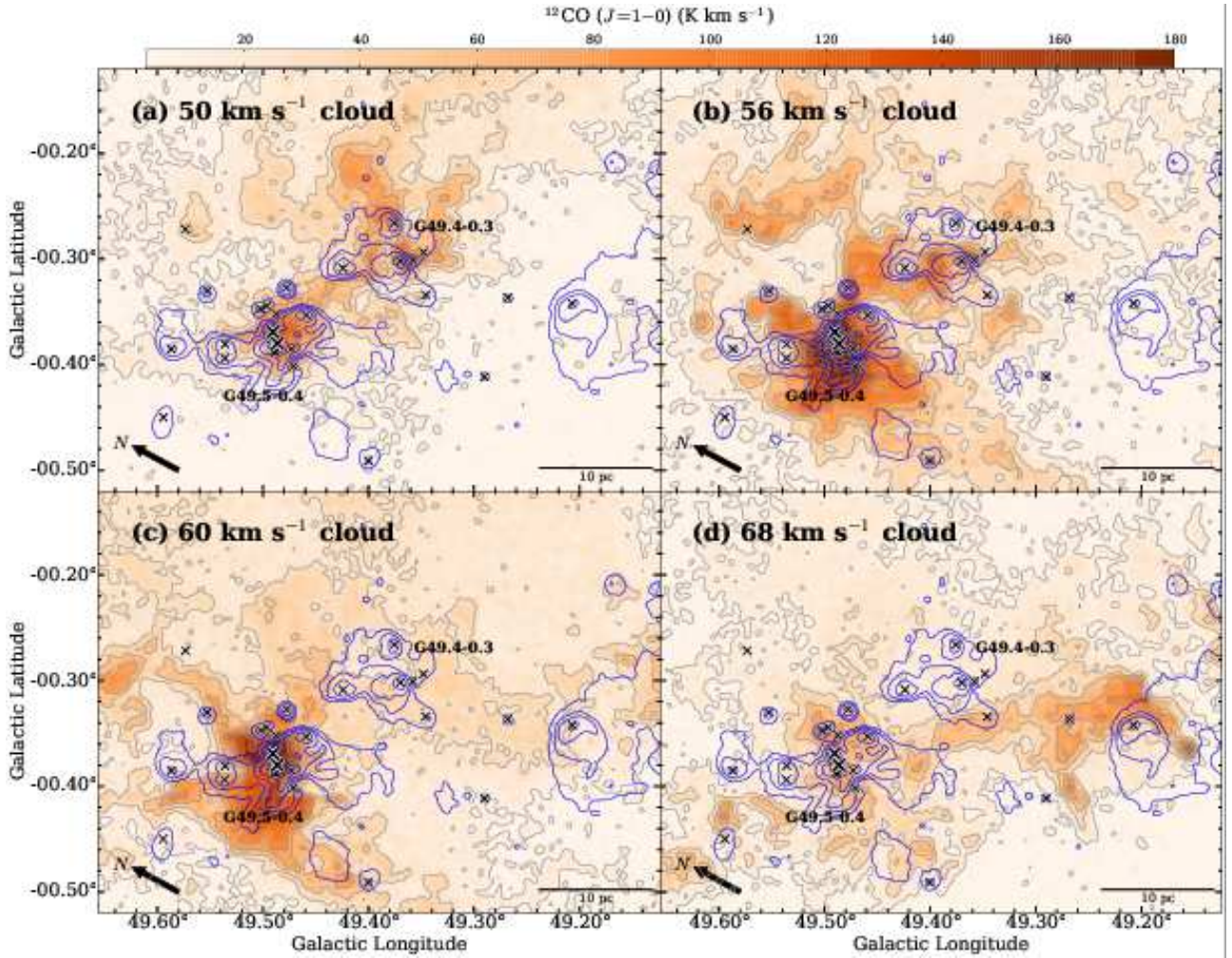


Fig. 5: The ^{12}CO ($J=1-0$) integrated intensity distributions of the (a) 50, (b) 56, (c) 60, and (d) 68 km s^{-1} clouds, with the integration ranges of 46.9–52.1, 52.8–58.6, 59.3–64.5, and 65.1–71.0 km s^{-1} , respectively. The gray contours are plotted with 6σ (20 K km s^{-1}) intervals starting from the 3σ (10 K km s^{-1}) level. The blue contours show the THOR 21 cm radio continuum emission combined with the VGPS data (Beuther et al. 2016; Stil et al. 2006), and are plotted from 0.06 to 3.0 Jy str^{-1} with logarithm step. The angular resolution of the THOR data combined with the VGPS is $25''$. The crosses represent HII regions listed in Mehringer (1994).

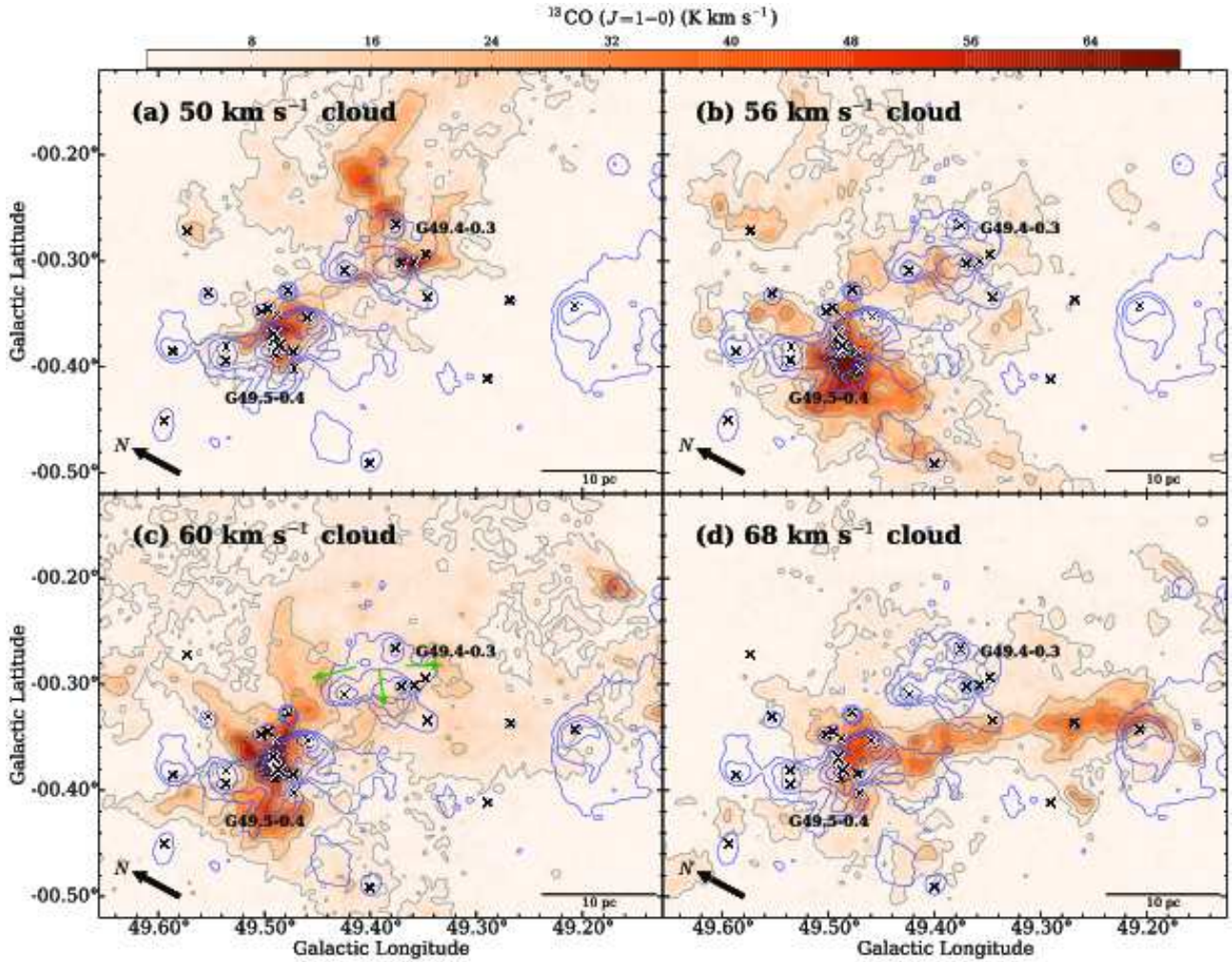


Fig. 6: Same as Figure 5 but for the $^{13}\text{CO } (J=1-0)$ emissions. The gray contours are plotted with 6σ (10 K km s^{-1}) intervals starting from the 3σ (5 K km s^{-1}) level.

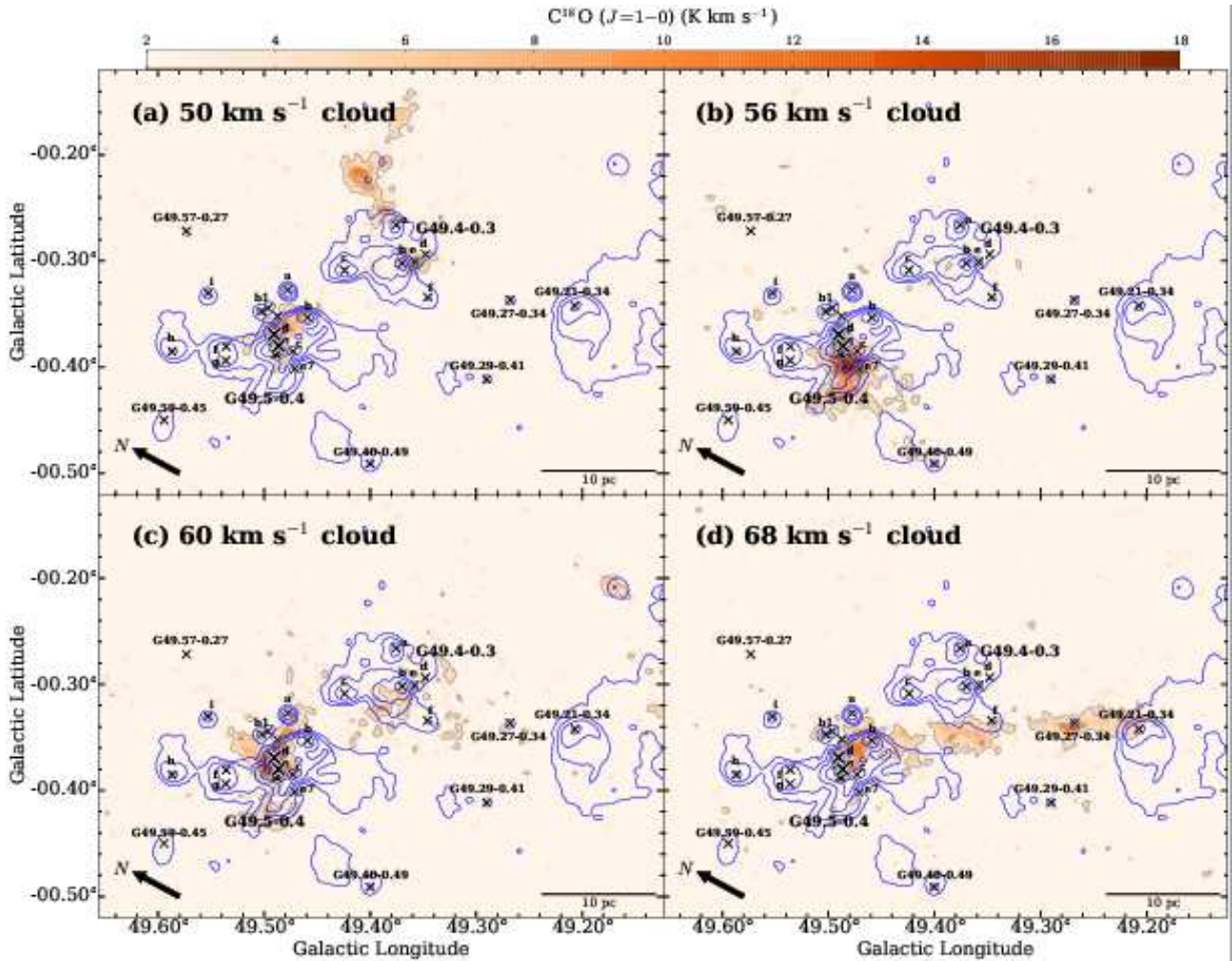


Fig. 7: Same as Figure 5 but for the $C^{18}O (J=1-0)$ emissions. The gray contours are plotted with 3σ ($4 K km s^{-1}$) intervals starting from the 3σ ($4 K km s^{-1}$) level.

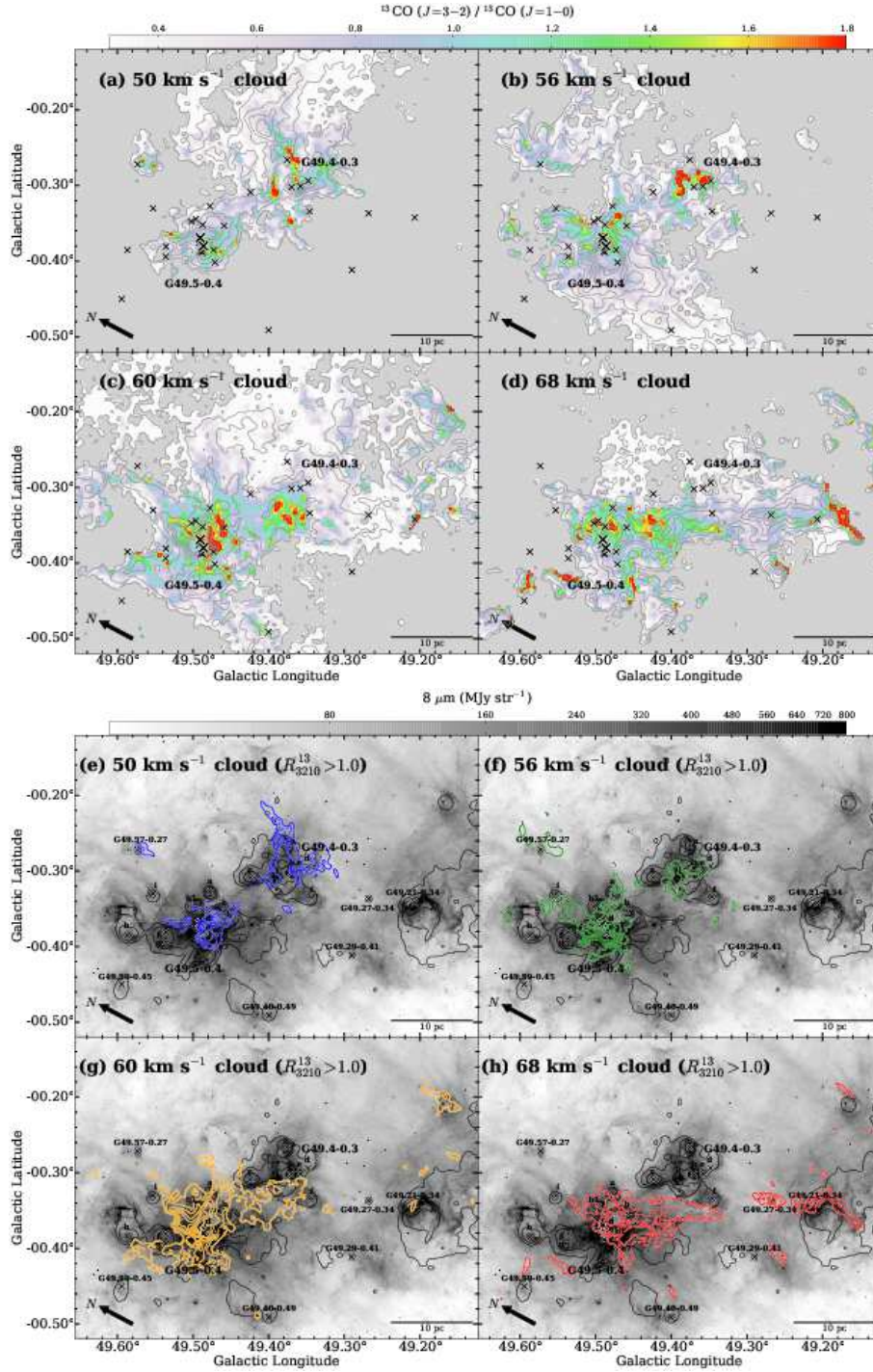


Fig. 8: (a–d) The R_{3210}^{13} distributions of the four clouds. The contours indicate $^{13}\text{CO} (J=1-0)$, and are plotted with 6σ (10 K km s^{-1}) intervals starting from the 6σ (10 K km s^{-1}) level for (a)–(c), and 6σ (5 K km s^{-1}) intervals starting from the 5σ (8 K km s^{-1}) level for (d), respectively. The associated errors of R_{3210}^{13} for each pixels are presented in Figure 20 in Appendix 2. (e–h) Spatial distributions of the high- R_{3210}^{13} gas are shown in the colored contour maps, where the high- R_{3210}^{13} data was made by integrating only the voxels having $R_{3210}^{13} > 1.0$. The colored contours are plotted at the same levels as in (a)–(d). The background image indicates the *Spitzer* $8 \mu\text{m}$ image, while the black contours represent the 21 cm continuum emissions plotted at the same levels as those in Figure 5. Crosses are the same as those in Figure 5.

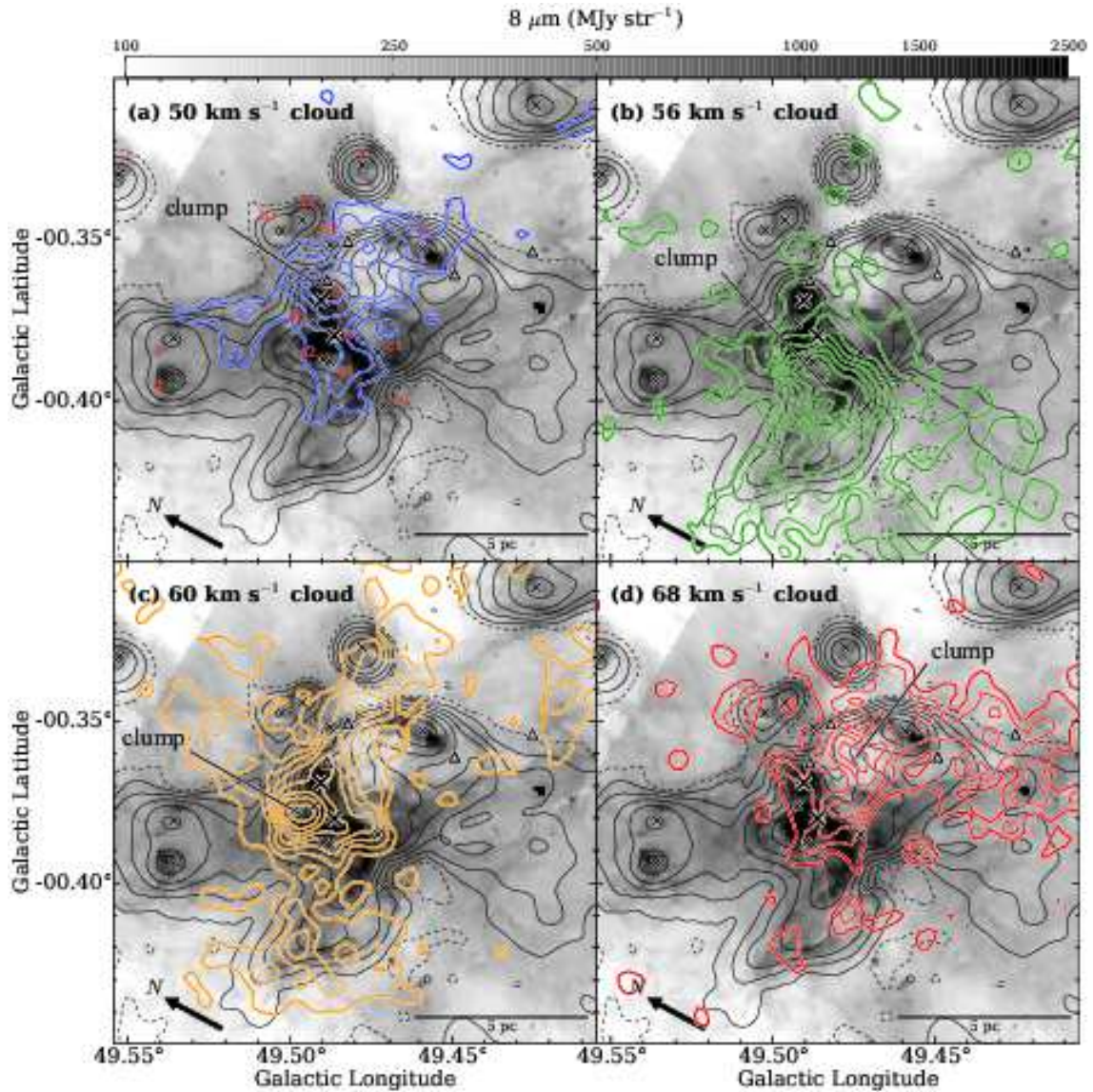


Fig. 9: C^{18}O ($J=1-0$) integrated intensity distributions of the four velocity clouds in G49.5-0.4 are presented as colored contour maps superimposed on the *Spitzer* $8\ \mu\text{m}$ image (Carey et al. 2009). The colored contours are plotted with $2\ \text{K km s}^{-1}$ intervals starting from the $3\ \text{K km s}^{-1}$ level where the RMS noise level of the image is $\sim 1.5\ \text{K km s}^{-1}$. The HII regions listed in Table 1 are depicted by crosses, and the massive young stars identified by Saral et al. (2017) are plotted with triangles. The black contours show the 21 cm continuum emissions plotted from 0.03 (dashed lines) to $3.0\ \text{Jy str}^{-1}$ with logarithm step.

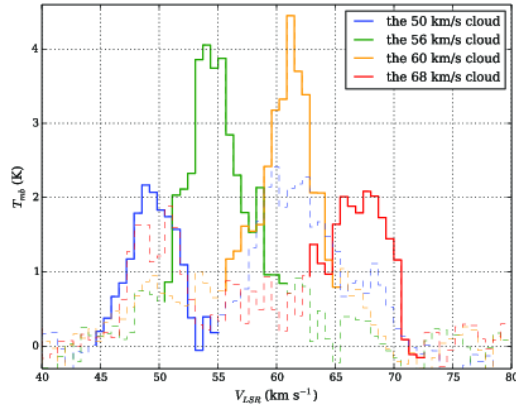


Fig. 10: The C^{18}O ($J=1-0$) spectra at the peak position (see Table 3) of each the clump embedded in the 50 km s^{-1} (blue), the 56 km s^{-1} (green), the 60 km s^{-1} (orange), and the 68 km s^{-1} (red) cloud. Velocities outside $\pm 5 \text{ km s}^{-1}$ of each peak of the clump are plotted with dashed lines.

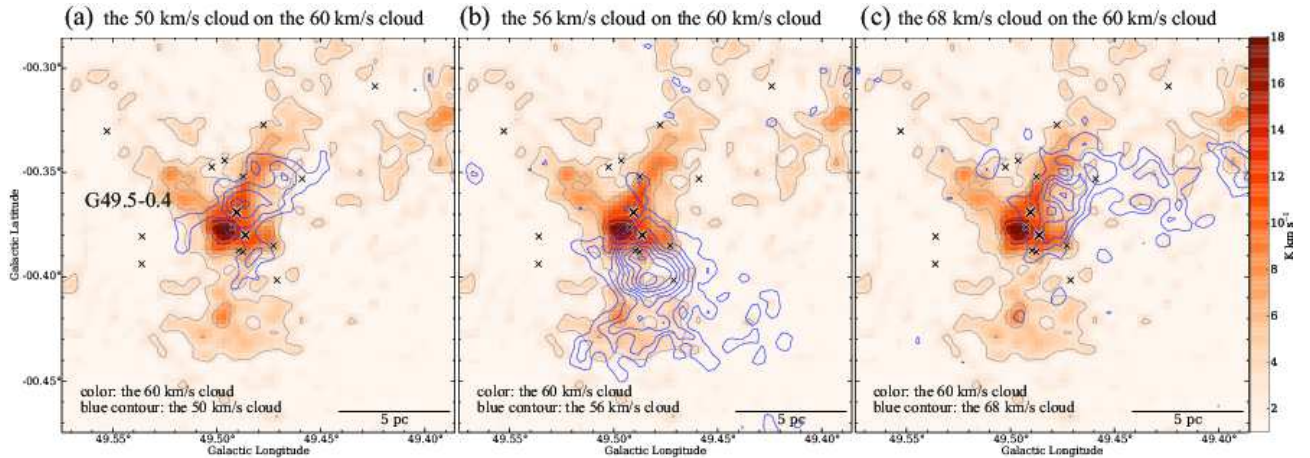


Fig. 11: (a) The C^{18}O ($J=1-0$) integrated intensity distributions of the 60 km s^{-1} cloud. Overlaid blue contours show the C^{18}O ($J=1-0$) integrated intensity distributions of the 50 km s^{-1} cloud, and are plotted with 1.5σ (2 K km s^{-1}) intervals starting from the 3σ (4 K km s^{-1}) level. The HII regions listed in Table 1 are denoted by crosses. (b) The same as (a), but the blue contours show the C^{18}O ($J=1-0$) integrated intensity distributions of the 56 km s^{-1} cloud. (c) The same as (a), but the blue contours show the C^{18}O ($J=1-0$) integrated intensity distributions of the 68 km s^{-1} cloud.

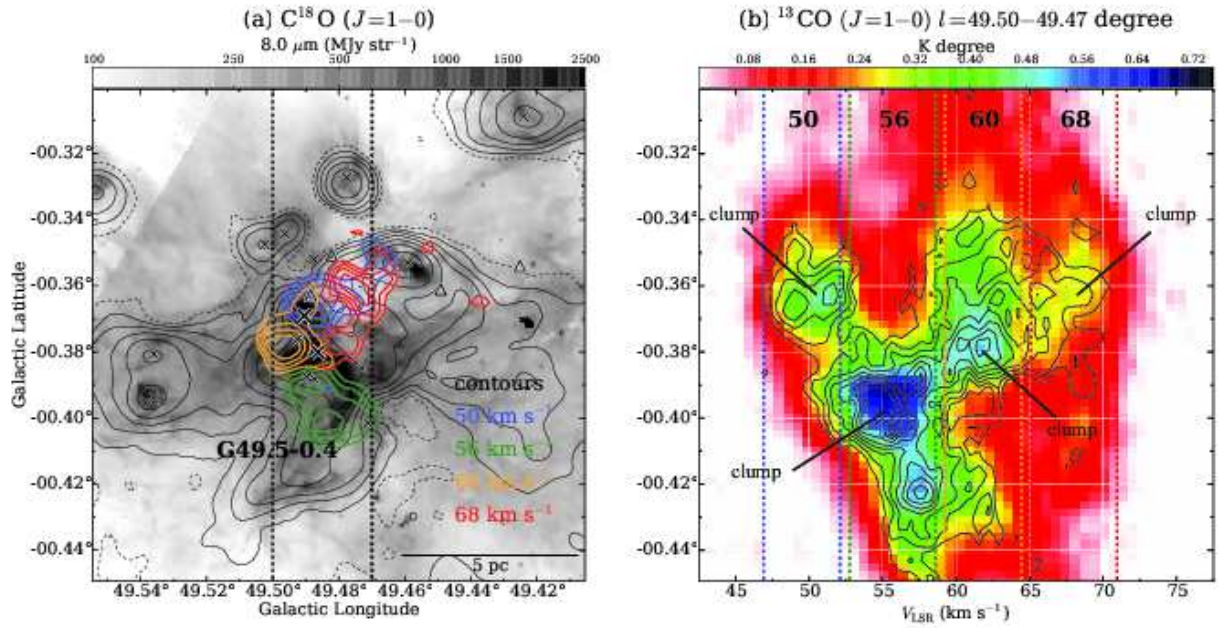


Fig. 12: (a) The contour maps of the $C^{18}O$ ($J=1-0$) emissions of the four clouds around G49.5-0.4 are plotted superimposed on the *Spitzer* $8\mu\text{m}$ image and 21 cm contour map. The $C^{18}O$ ($J=1-0$) contours are plotted at 60, 70, 80, and 90 % of the peak intensities of the four clumps. The black contours show the 21 cm continuum emissions plotted from 0.03 (dashed lines) to 3.0Jy str^{-1} with logarithm step. (b) Velocity–Galactic Latitude (v – b) diagram of the ^{13}CO ($J=1-0$) (color) and $C^{18}O$ ($J=1-0$) emissions (contours) towards G49.5-0.4 integrated over $l = 49^{\circ}50-49^{\circ}47$, where the contours are plotted with 5σ (0.03 K degrees) intervals starting from the 5σ (0.03 K degrees) level. The vertical dashed lines show the integration ranges of the four clouds presented in Figures 9 and 12(a).

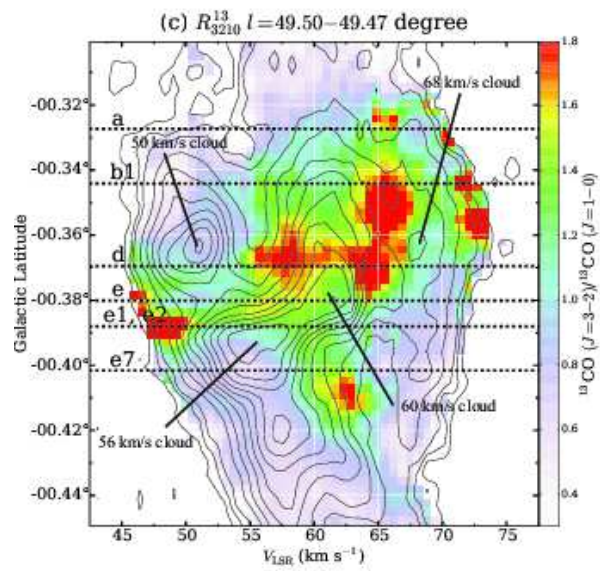


Fig. 12: Continued. (c) The v - b diagram of the R_{3210}^{13} distributions toward G49.5-0.4 integrated over $l = 49^{\circ}50-49^{\circ}47$. The contours show the intensity of the $^{13}\text{CO } (J=1-0)$. The horizontal dashed lines indicate the position of the compact HII regions G49.5-0.4a, b, d, e, e1, e2, and e7.

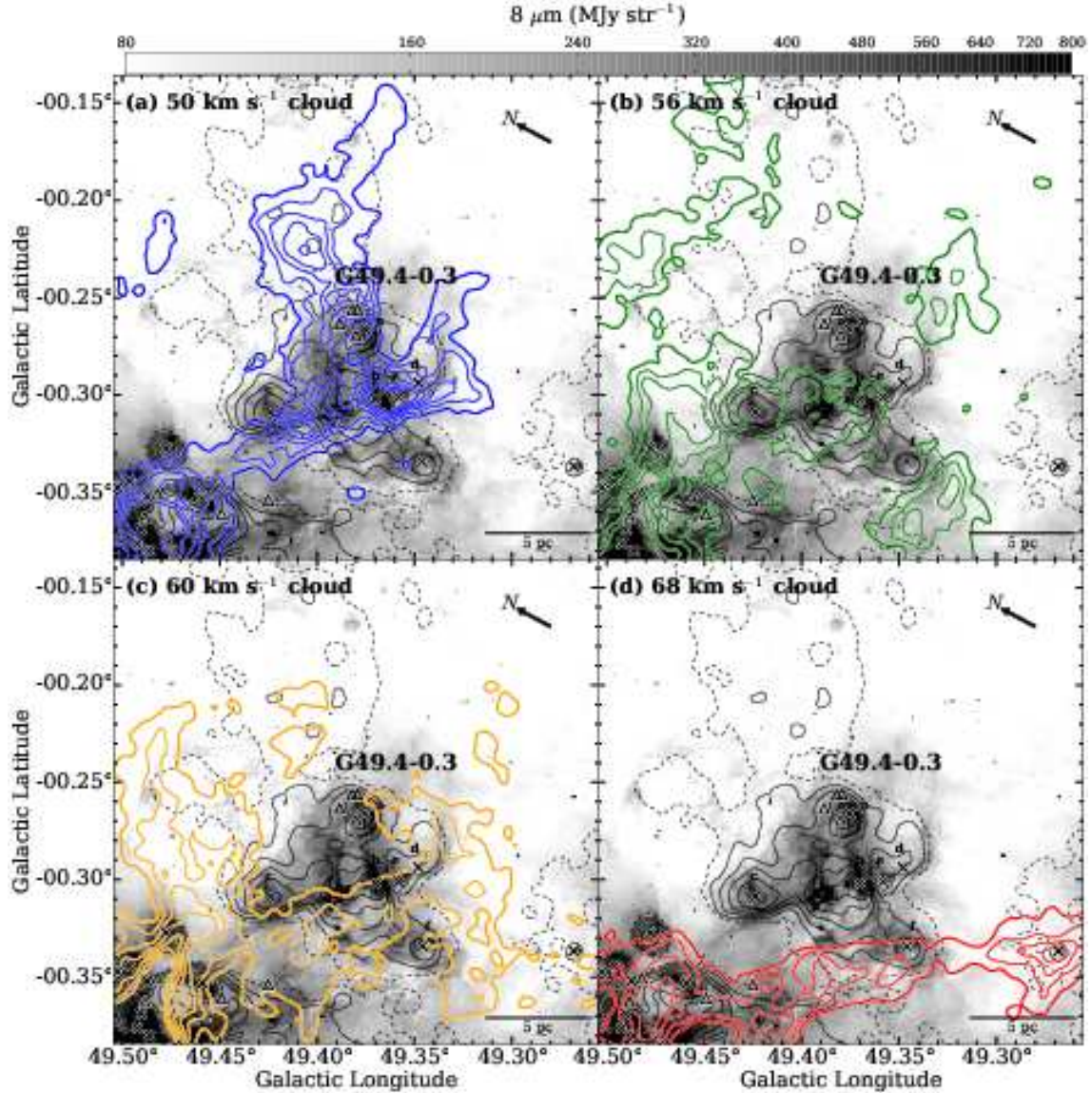


Fig. 13: ^{13}CO ($J=1-0$) integrated intensity distributions of the four velocity clouds in G49.4-0.3 are presented as colored contour maps superimposed on the *Spitzer* $8\ \mu\text{m}$ image (Carey et al. 2009). Velocity ranges of the ^{13}CO emissions in the panels (a)–(d) are 46.9–55.4, 55.4–59.3, 59.3–64.5, and 64.5–71.0 km s^{-1} , and contours are plotted with 8 K km s^{-1} intervals starting from the 18 K km s^{-1} level for (a), 4 K km s^{-1} intervals starting from the 4 K km s^{-1} level for (b), 6 K km s^{-1} intervals starting from the 12 K km s^{-1} level for (c), and 8 K km s^{-1} intervals starting from the 12 K km s^{-1} level for (d), respectively, where the RMS noise level of the images are $\sim 1.5\ \text{K km s}^{-1}$. Black contours show the 21 cm emissions plotted at the same levels as those in Figure 5. The HII regions listed in Table 1 are depicted by crosses, and the MYSOs identified by Saral et al. (2017) are plotted with triangles.

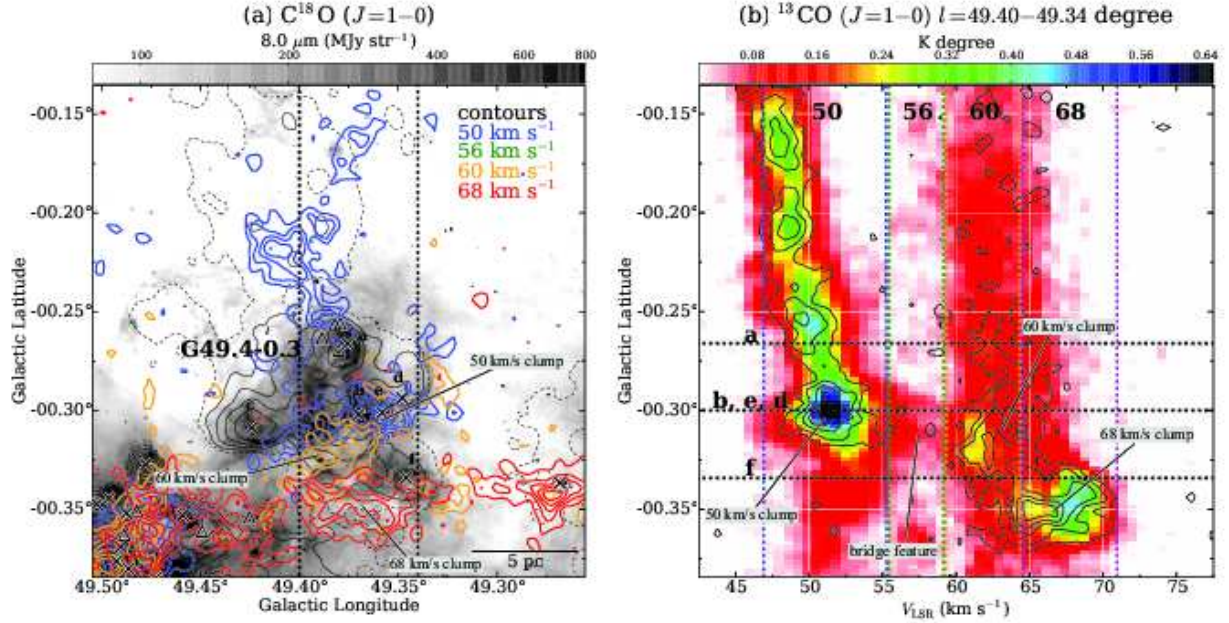


Fig. 14: (a) The colored contour maps (blue, green, orange, and red) of the $C^{18}O$ emissions of the four clouds around G49.4-0.3 are plotted superimposed on the *Spitzer* $8\mu m$ image and 21 cm contour map (black). $C^{18}O$ contours are plotted with 2 K km s^{-1} intervals starting from the 3σ (4 K km s^{-1}) level. Crosses represent compact HII regions listed in Mehringer (1994) (Table 1), while the MYSO identified by Saral et al. (2017) is plotted with triangle. (b) Velocity–Galactic Latitude ($v-b$) diagram of ^{13}CO ($J=1-0$) integrated over $l = 49^{\circ}.40-49^{\circ}.34$. Contours indicate the $C^{18}O$ ($J=1-0$) emissions and are plotted with 3σ (0.02 K degrees) intervals starting from the 3σ (0.02 K degrees) level. Horizontal dashed lines indicate the positions of compact HII regions, while the vertical dashed lines show the integration ranges of the four clouds presented in Figures 13 and 14(a).

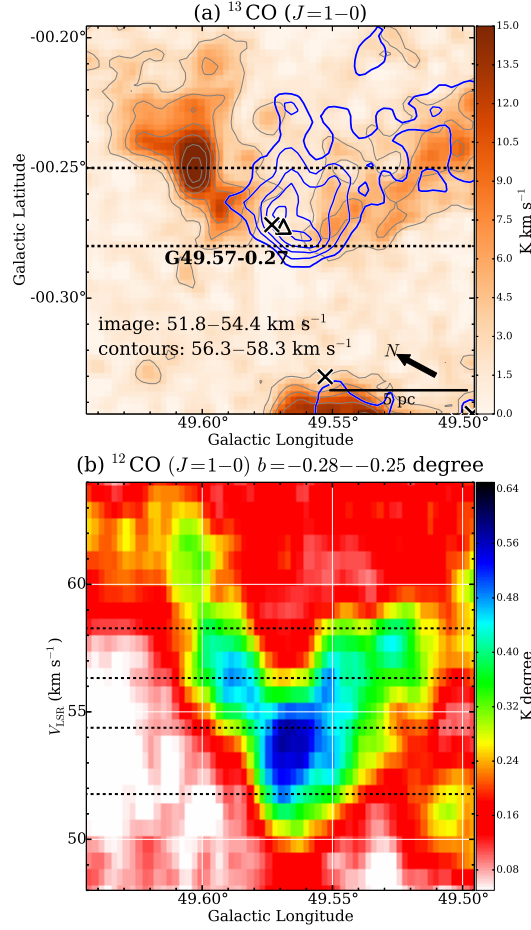


Fig. 15: (a) The complementary distributions of the two velocity components toward G49.57-0.27. The color scale shows ^{13}CO ($J=1-0$) for $56.3-58.3 \text{ km s}^{-1}$, while the blue contours show ^{13}CO ($J=1-0$) for $51.8-54.4 \text{ km s}^{-1}$. The blue contours are plotted with 3σ (4 K km s^{-1}) intervals starting from the 5σ (6 K km s^{-1}) level. Crosses represent compact HII regions listed in Mehringer (1994) (Table 1), while the MYSO identified by Saral et al. (2017) is plotted with triangle. (b) Galactic Longitude-velocity diagram of the ^{12}CO ($J=1-0$) emission toward G49.57-0.27. The integration range in b is shown in (a) with vertical dashed lines.

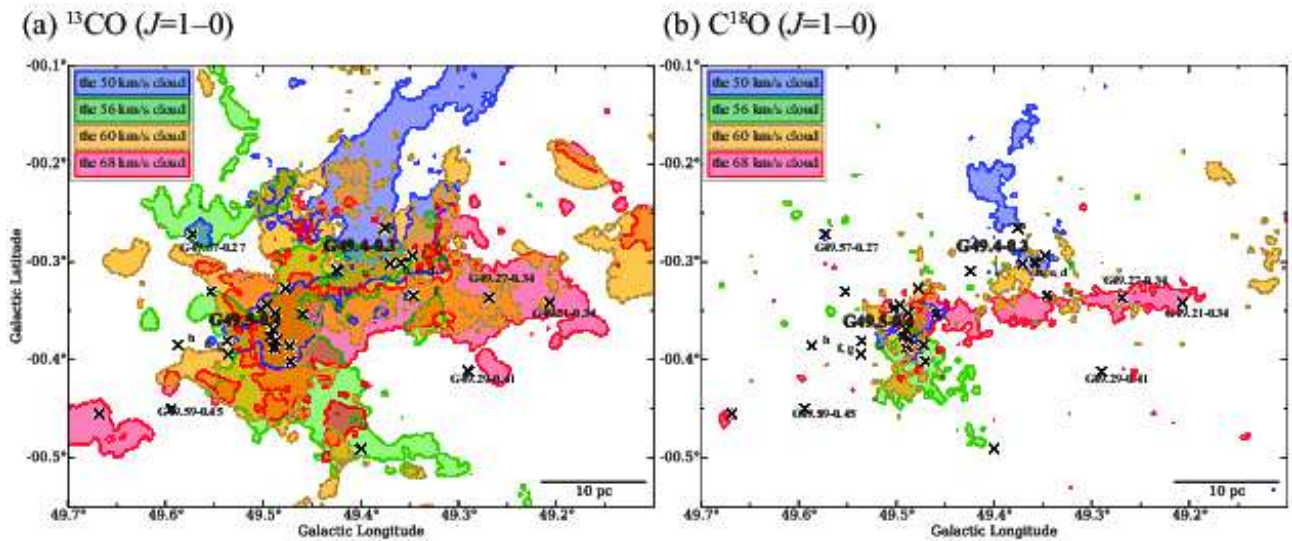


Fig. 16: (a) The ^{13}CO ($J=1-0$) integrated intensity distributions of the 50 (blue contour), 56 (green contour), 60 (orange contour with gray dashed-contour), and 68 km s^{-1} clouds (red contour). The integration ranges is the same as Figure 6, and the contour level is 10, 10, 10, and 8 K km s^{-1} , respectively. The crosses represent HII regions listed in Mehringer (1994). (b) Same as (a), but for the C^{18}O ($J=1-0$) integrated intensity distributions.

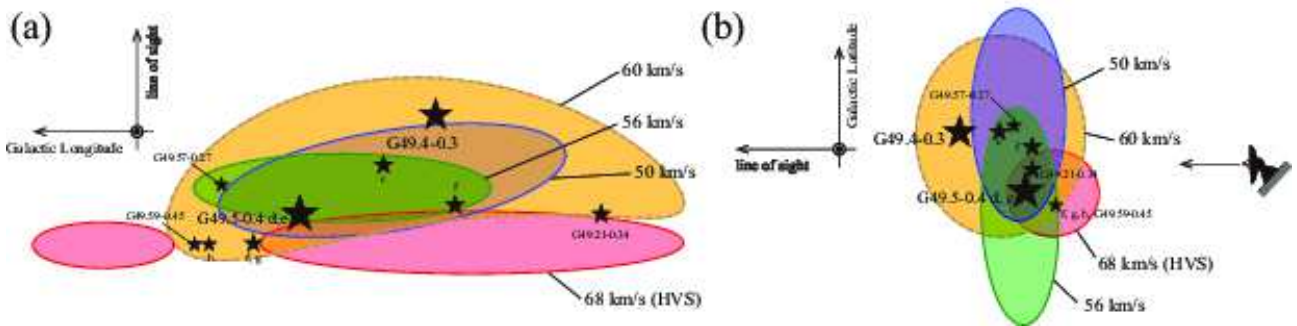


Fig. 17: (a) The schematic pictures of the distributions of the molecular gas in W51A based on Ginsburg et al. (2015) as viewed from the Galactic north pole. Star markers indicate the positions of the representative HII regions in W51A. (b) Same as (a), but as viewed from the Galactic eastern side.

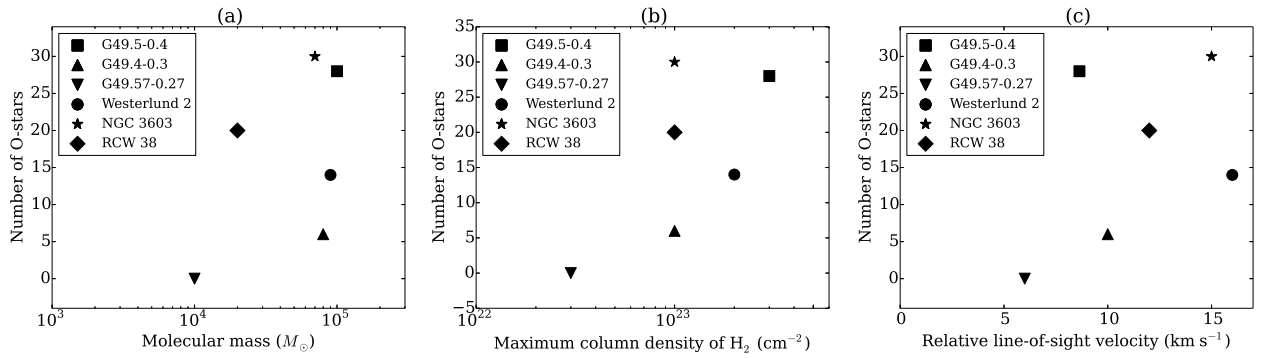


Fig. 18: Correlation between (a) the molecular mass and the number of O-stars, (b) the $N_{\max}(H_2)$ and the number of O-stars, and (c) the relative line-of-sight velocity and the number of O-stars. In (a) and (b), the molecular masses and the $N_{\max}(H_2)$ of the largest cloud in the each HII region are plotted. In (c), the geometric mean of the relative velocities is plotted for G49.5-0.4.

Acknowledgments

This study was financially supported by Grants-in-Aid for Scientific Research (KAKENHI) of the Japanese society for the Promotion of Science (JSPS; grant numbers 15K17607, 17H06740, and 18K13580). The authors would like to thank the all members of the 45-m group of Nobeyama Radio Observatory for support during the observation. Data analysis was carried out on the open use data analysis computer system at the Astronomy Data Center (ADC), of the National Astronomical Observatory of Japan (NAOJ), and made use of Astropy, a community-developed core Python package for Astronomy (Astropy Collaboration et al. 2013), APLpy, an open-source plotting package for Python (Robitaille & Bressert 2012), astrodendro, a Python package to compute dendrograms of Astronomical data (Rosolowsky et al. 2008), and SCIMES, a Python package to find relevant structures into dendrograms of molecular gas emission using the spectral clustering approach (Colombo et al. 2015). The authors also would like to thank NASA, National Radio Astronomy Observatory (NRAO), and Dr. H. Parsons for providing FITS data of *Spitzer* Space Telescope and the JCMT, and VGPS, respectively.

References

- Anathpindika, S. V. 2010, MNRAS, 405, 1431
- Anderson, L. D., Bania, T. M., Balser, D. S., et al. 2014, ApJS, 212, 1
- Arnal, E. M., & Goss, W. M. 1985, A&A, 145, 369
- Astropy Collaboration, Robitaille, T. P., Tollerud, E. J., et al. 2013, A&A, 558, A33
- Beuther, H., Bihl, S., Rugel, M., et al. 2016, A&A, 595, A32
- Bieging, J. 1975, H II regions and related topics, 42, 443
- Bonnell, I. A., Bate, M. R., Clarke, C. J., & Pringle, J. E. 2001, MNRAS, 323, 785
- Burton, W. B., & Shane, W. W. 1970, The Spiral Structure of our Galaxy, 38, 397
- Cardelli, J. A., Clayton, G. C., & Mathis, J. S. 1989, ApJ, 345, 245
- Carey, S. J., Noriega-Crespo, A., Mizuno, D. R., et al. 2009, PASP, 121, 76
- Carpenter, J. M., & Sanders, D. B. 1998, AJ, 116, 1856
- Colombo, D., Rosolowsky, E., Ginsburg, A., Duarte-Cabral, A., & Hughes, A. 2015, MNRAS, 454, 2067
- Dickman, R. L. 1978, ApJS, 37, 407
- Frerking, M. A., Langer, W. D., & Wilson, R. W. 1982, ApJ, 262, 590
- Fukui, Y., Ohama, A., Hanaoka, N., et al. 2014, ApJ, 780, 36
- Fukui, Y., Harada, R., Tokuda, K., et al. 2015, ApJL, 807, L4
- Fukui, Y., Torii, K., Ohama, A., et al. 2016, ApJ, 820, 26
- Fukui, Y., Tsuge, K., Sano, H., et al. 2017, PASJ, 69, L5
- Fukui, Y., Kohno, M., Yokoyama, K., et al. 2017, arXiv:1706.05768
- Fukui, Y., Torii, K., Hattori, Y., et al. 2018, ApJ, 859, 166
- Furukawa, N., Dawson, J. R., Ohama, A., et al. 2009, ApJL, 696, L115
- Ginsburg, A., Bally, J., Battersby, C., et al. 2015, A&A, 573, A106

Goldreich, P., & Kwan, J. 1974, *ApJ*, 189, 441

Habe, A., & Ohta, K. 1992, *PASJ*, 44, 203

Haworth, T. J., Shima, K., Tasker, E. J., et al. 2015, *MNRAS*, 454, 1634

Haworth, T. J., Tasker, E. J., Fukui, Y., et al. 2015, *MNRAS*, 450, 10

Hayashi, K., Sano, H., Enokiya, R., et al. 2017, arXiv:1706.05871

Indebetouw, R., Mathis, J. S., Babler, B. L., et al. 2005, *ApJ*, 619, 931

Inoue, T., & Fukui, Y. 2013, *ApJL*, 774, L31

Inoue, T., Hennebelle, P., Fukui, Y., et al. 2017, arXiv:1707.02035

Kang, M., Bieging, J. H., Povich, M. S., & Lee, Y. 2009, *ApJ*, 706, 83

Kang, M., Bieging, J. H., Kulesa, C. A., et al. 2010, *ApJS*, 190, 58

Kawamura, A., Onishi, T., Yonekura, Y., et al. 1998, *ApJS*, 117, 387

Kim, H., Nakajima, Y., Sung, H., Moon, D.-S., & Koo, B.-C. 2007, *Journal of Korean Astronomical Society*, 40, 17

Kobayashi, M. I. N., Kobayashi, H., Inutsuka, S.-i., & Fukui, Y. 2017, arXiv:1708.07952

Kohno, M., Torii, K., Tachihara, K., et al. 2017, arXiv:1706.07964

Koo, B.-C. 1997, *ApJS*, 108, 489

Koo, B.-C., & Moon, D.-S. 1997, *ApJ*, 475, 194

Koo, B.-C., & Moon, D.-S. 1997, *ApJ*, 485, 263

Koo, B.-C. 1999, *ApJ*, 518, 760

Krumholz, M. R., Klein, R. I., McKee, C. F., Offner, S. S. R., & Cunningham, A. J. 2009, *Science*, 323, 754

Kumar, M. S. N., Kamath, U. S., & Davis, C. J. 2004, *MNRAS*, 353, 1025

Kuno, N., et al. 2011, *General Assembly and Scientific Symposium, XXXth URSI, JP2-19*

Leung, C.-M., & Liszt, H. S. 1976, *ApJ*, 208, 732

Leung, C. M., Herbst, E., & Huebner, W. F. 1984, *ApJS*, 56, 231

Makai, Z., Anderson, L. D., Mascoop, J. L., & Johnstone, B. 2017, *ApJ*, 846, 64

Mehring, D. M. 1994, *ApJS*, 91, 713

Minamidani, T., Nishimura, A., Miyamoto, Y., et al. 2016, *Proc. SPIE*, 9914, 99141Z

Nishimura, A., Minamidani, T., Umamoto, T., et al. 2017a, arXiv:1706.06956

Nishimura, A., Costes, J., Inaba, T., et al. 2017b, arXiv:1706.06002

Ohama, A., Dawson, J. R., Furukawa, N., et al. 2010, *ApJ*, 709, 975

Ohama, A., Kono, M., Tsutsumi, D., et al. 2017, arXiv:1706.05659

Ohama, A., Tsutsumi, D., Sano, H., et al. 2017, arXiv:1706.05652

Oka, T., Nagai, M., Kamegai, K., Tanaka, K., & Kuboi, N. 2007, *PASJ*, 59, 15

Okumura, S.-i., Mori, A., Nishihara, E., Watanabe, E., & Yamashita, T. 2000, *ApJ*, 543, 799

Okumura, S.-I., Miyawaki, R., Sorai, K., Yamashita, T., & Hasegawa, T. 2001, PASJ, 53, 793

Pankonin, V., Payne, H. E., & Terzian, Y. 1979, A&A, 75, 365

Parsons, H., Thompson, M. A., Clark, J. S., & Chrysostomou, A. 2012, MNRAS, 424, 1658

Rengarajan, T. N., Cheung, L. H., Fazio, G. G., Shivanandan, K., & McBreen, B. 1984, ApJ, 286, 573

Robitaille, T., & Bressert, E. 2012, Astrophysics Source Code Library, ascl:1208.017

Rosolowsky, E. W., Pineda, J. E., Kauffmann, J., & Goodman, A. A. 2008, ApJ, 679, 1338

Saral, G., Hora, J. L., Audard, M., et al. 2017, ApJ, 839, 108

Sano, H., Enokiya, R., Hayashi, K., et al. 2017, arXiv:1706.05763

Sato, M., Reid, M. J., Brunthaler, A., & Menten, K. M. 2010, ApJ, 720, 1055

Shetty, R., Glover, S. C., Dullemond, C. P., & Klessen, R. S. 2011, MNRAS, 412, 1686

Shimoikura, T., Dobashi, K., Saito, H., et al. 2013, ApJ, 768, 72

Spitzer, L. 1978, Physical processes in the interstellar medium, by Lyman Spitzer. New York Wiley-Interscience, 1978. 333 p.,

Stil, J. M., Taylor, A. R., Dickey, J. M., et al. 2006, AJ, 132, 1158

Takahira, K., Tasker, E. J., & Habe, A. 2014, ApJ, 792, 63

Takahira, K., Shima, K., Tasker, E. J., & Habe, A. 2017, arXiv:1706.08656

Tan, J. C., Beltrán, M. T., Caselli, P., et al. 2014, Protostars and Planets VI, 149

Torii, K., Enokiya, R., Sano, H., et al. 2011, ApJ, 738, 46

Torii, K., Hasegawa, K., Hattori, Y., et al. 2015, ApJ, 806, 7

Torii, K., Hattori, Y., Hasegawa, K., et al. 2017, ApJ, 835, 142

Torii, K., Hattori, Y., Matsuo, M., et al. 2017, arXiv:1706.07164

Tsuboi, M., Miyazaki, A., & Uehara, K. 2015, PASJ, 67, 109

Tsutsumi, D., Ohama, A., Okawa, K., et al. 2017, arXiv:1706.05664

Umemoto, T., Minamidani, T., Kuno, N., et al. 2017, PASJ, 69, 78

Westerhout, G. 1958, Bull. Astron. Inst. Netherlands, 14, 215

White, R. E. 1977, ApJ, 211, 744

Wilson, T. L., & Rood, R. 1994, ARA&A, 32, 191

Wolfire, M. G., & Cassinelli, J. P. 1987, ApJ, 319, 850

Wynn-Williams, C. G., Becklin, E. E., & Neugebauer, G. 1974, ApJ, 187, 473

Zinnecker, H., & Yorke, H. W. 2007, ARA&A, 45, 481

Appendix 1 Velocity channel maps of the CO ($J=1-0$) emissions

In Figures 19(a)–(c), we presented velocity channel maps of the ^{12}CO ($J=1-0$), ^{13}CO ($J=1-0$) and C^{18}O ($J=1-0$) emissions at a velocity step of 3.25 km s^{-1} .

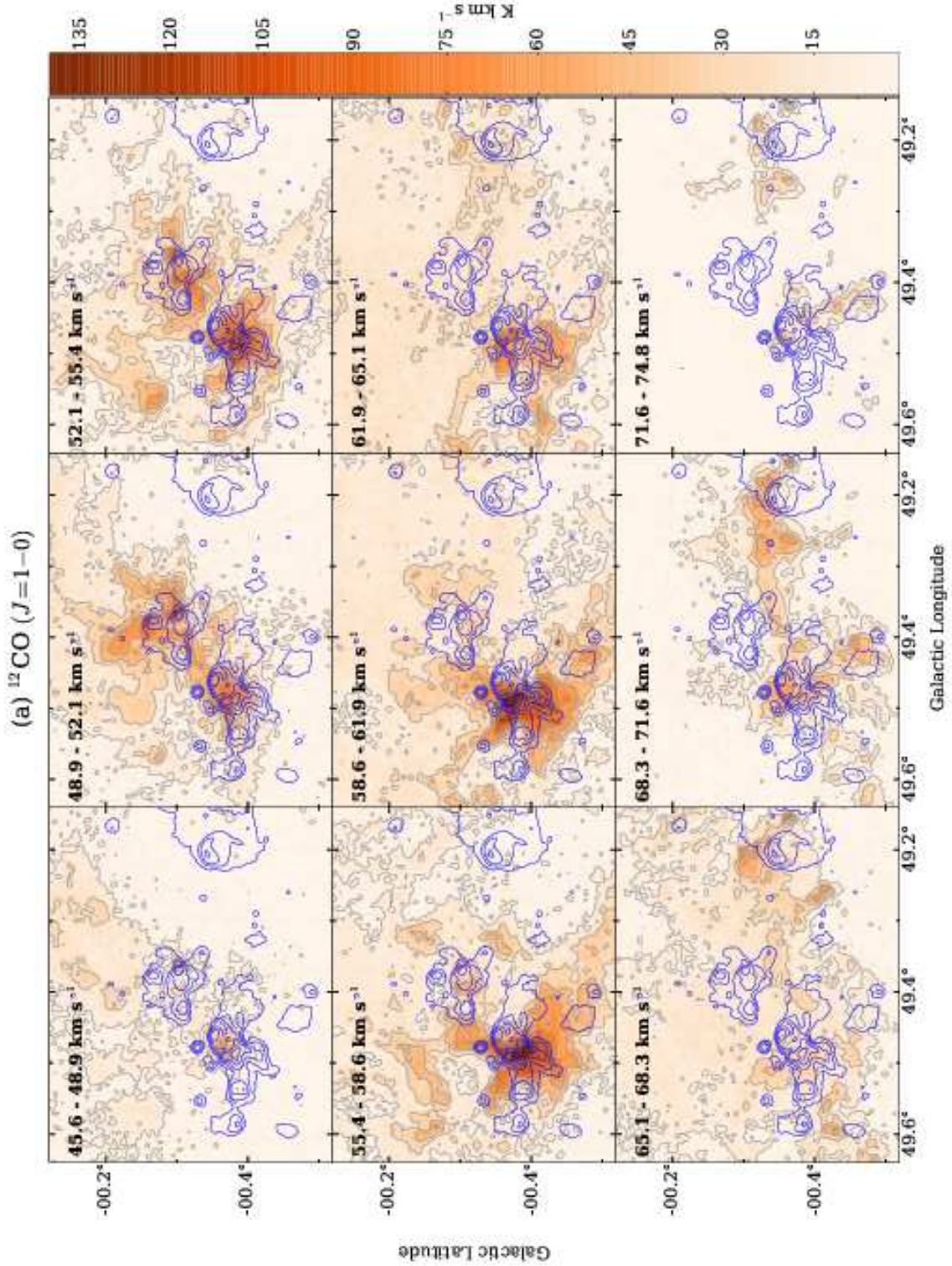


Fig. 19: The velocity channel maps of the ^{12}CO ($J=1-0$) emissions. The gray contours are plotted with 8σ (16 K km s^{-1}) intervals starting from the 4σ (8 K km s^{-1}) level. Integration range in each panel is presented in the top-left corner of the panel. The blue contours indicate the THOR 21 cm radio continuum emission combined with the VGPS data (Beuther et al. 2016; Stil et al. 2006), and are plotted from 0.03 (dashed lines) to 3.0 Jy str^{-1} with logarithm step. The angular resolution of the THOR data combined with the VGPS is $25''$.

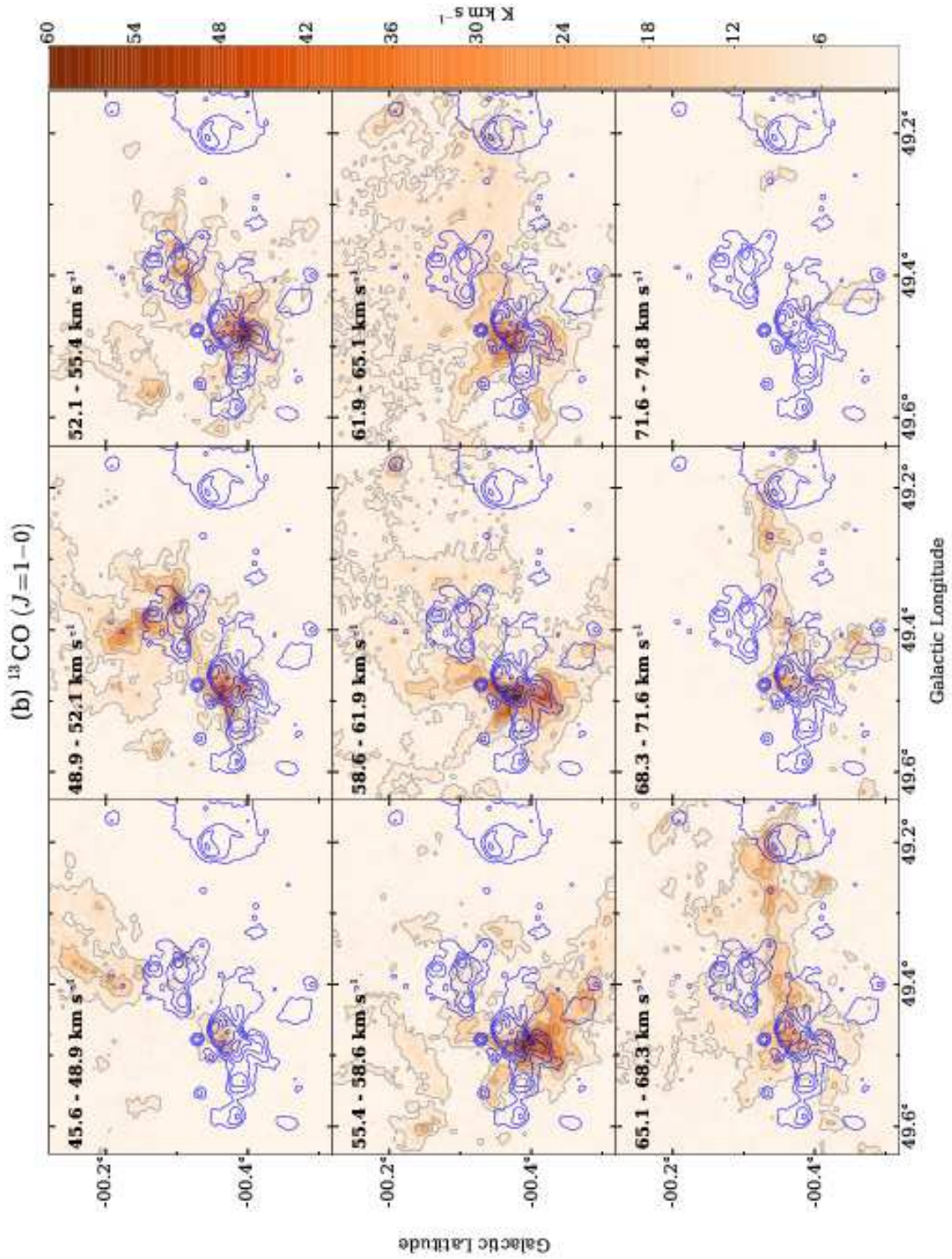


Fig. 19: (Continued.) Same as 19 but for ^{13}CO ($J=1-0$). The gray contours are plotted with 8σ (8 K km s^{-1}) intervals starting from the 4σ (4 K km s^{-1}) level.

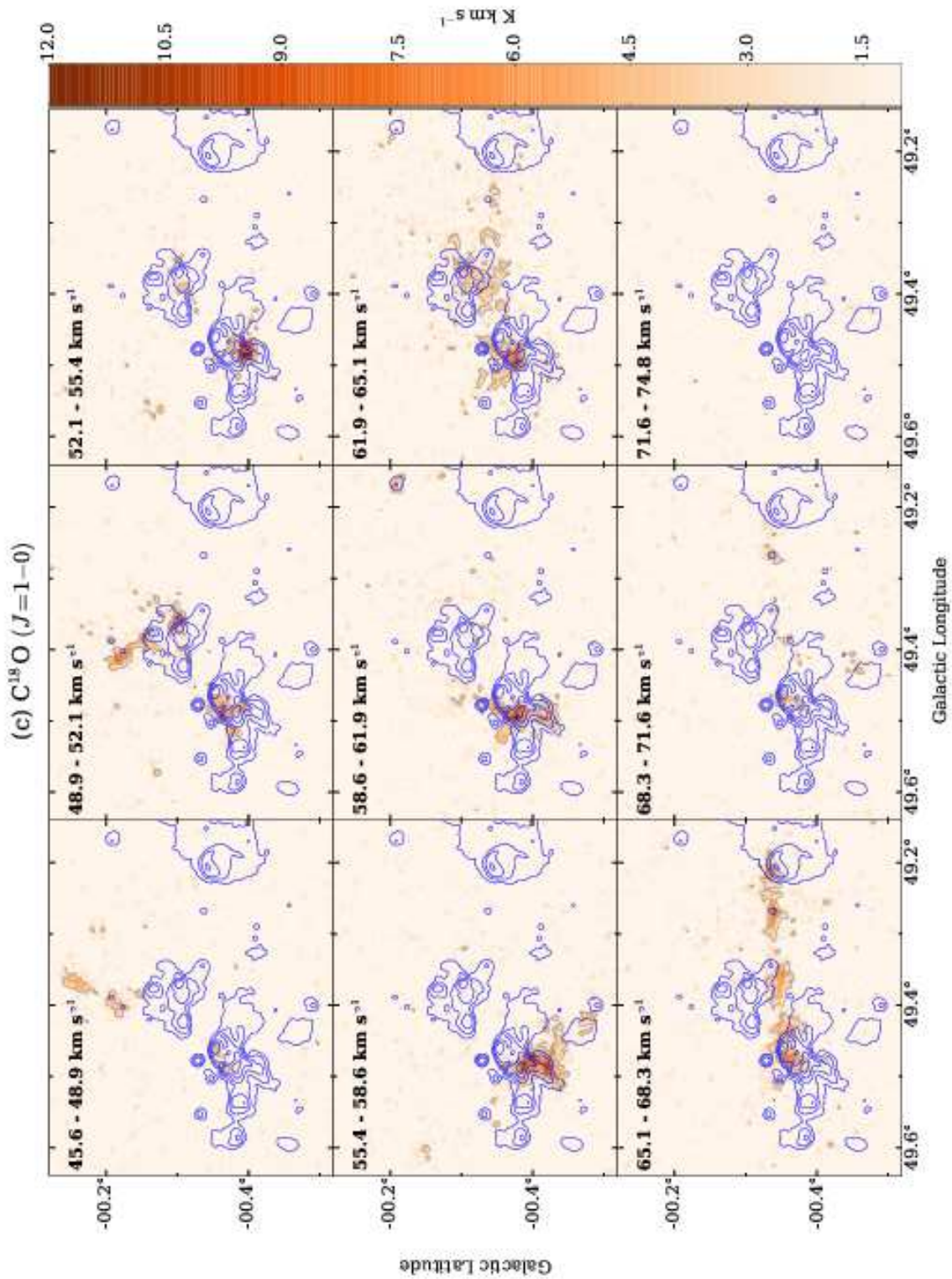


Fig. 19: (Continued.) Same as 19 but for $C^{18}O$ ($J=1-0$). The gray contours are plotted with 3σ (3 K km s^{-1}) intervals starting from the 3σ (3 K km s^{-1}) level.

Appendix 2 Errors associated with R_{3210}^{13}

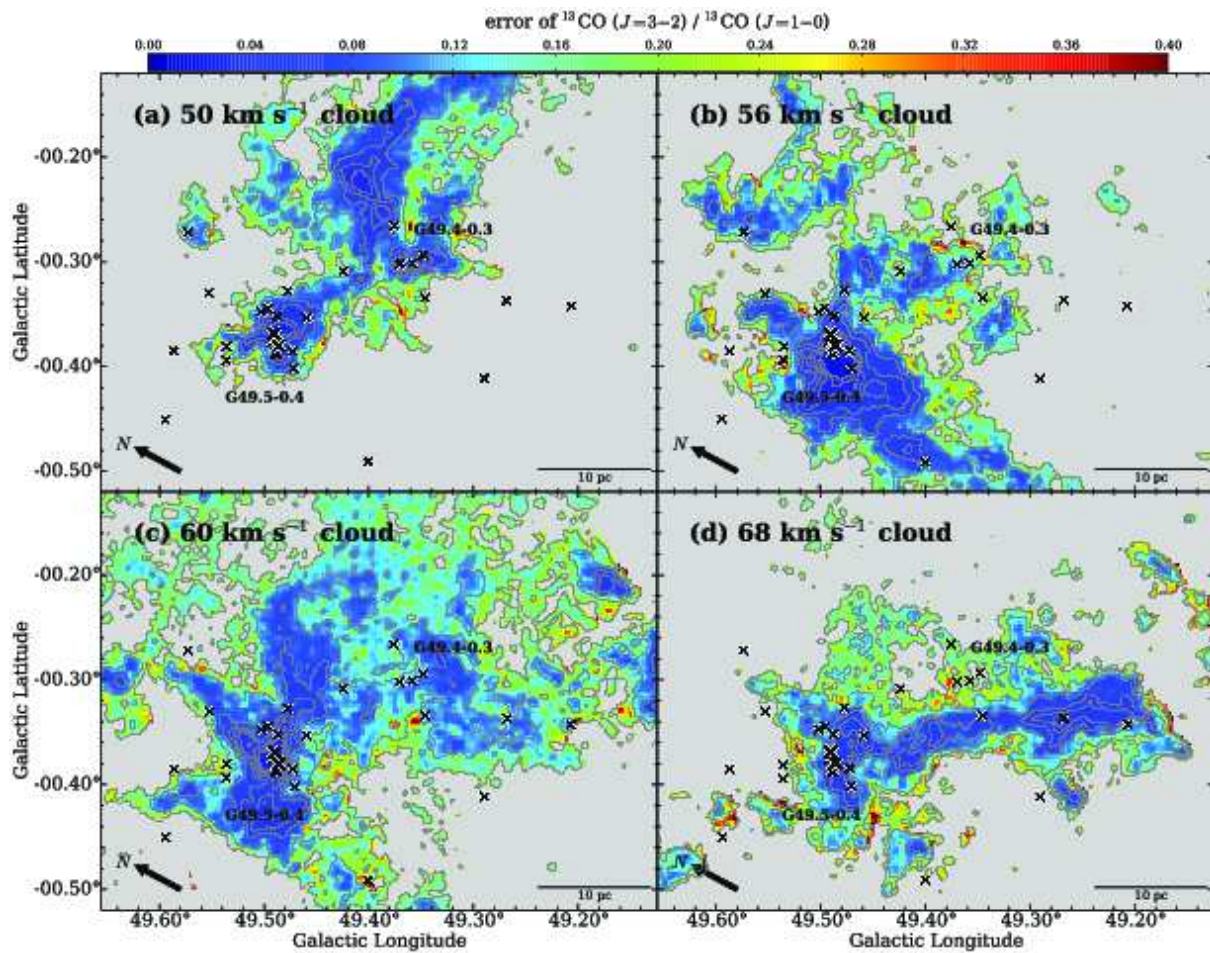


Fig. 20: The map of the error associated with R_{3210}^{13} (Figure 8(a)–(d)) for each pixels. The errors were estimated from the calibration error of the $^{13}\text{CO } (J=1-0)$ and $^{13}\text{CO } (J=3-2)$ data (15% and 10%, respectively).

Appendix 3 Large velocity gradient analysis

To investigate high-temperature gas in the molecular clouds of W51A, we utilize the large velocity gradient (LVG) calculations (e.g., Goldreich & Kwan 1974). The assumption of the uniform velocity gradient is not always valid in the molecular gas associated with HII regions. However radiative transfer calculations assuming a micro-turbulent cloud interacting with an HII region shows no significant difference from the LVG analysis (e.g., Leung & Liszt 1976; White 1977). We therefore adopt the LVG approximation in the present study. We here adopted the abundance ratios of $[\text{}^{12}\text{CO}]/[\text{}^{13}\text{CO}] = 77$ (Wilson & Rood 1994) and the fractional CO abundance to be $X(\text{CO}) = [\text{}^{12}\text{CO}]/[\text{H}_2] = 10^{-4}$ (e.g., Frerking et al. 1982; Leung et al. 1984). Two velocity gradient dv/dr of 5 and 10 $\text{km s}^{-1} \text{pc}^{-1}$ were adopted, by assuming a typical velocity width of individual velocity clouds, $\sim 3 \text{ km s}^{-1}$ and a full velocity width of the four velocity clouds, $\sim 30 \text{ km s}^{-1}$ (see Figure 4), multiplied by a typical size of the molecular gas components of $\sim 3 \text{ pc}$.

Figure 21 shows R_{3210}^{13} distributions calculated with LVG for different densities $n(\text{H}_2)$ as a function of kinetic temperature T_k of gas, indicating that R_{3210}^{13} is sensitive to gas temperature. In all the $n(\text{H}_2)$ cases, R_{3210}^{13} of higher than 1.0 corresponds to T_k of higher than $\sim 20 \text{ K}$. 20 K is significantly higher than typical temperature of molecular clouds without star formation, 10 K (Fukui et al. 2016).

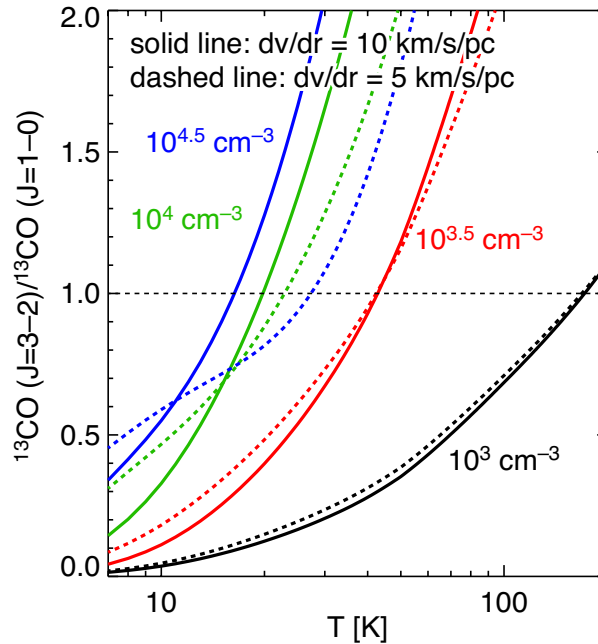


Fig. 21: Curves of R_{3210}^{13} as a function of T_k and $n(\text{H}_2)$, estimated using the LVG calculations. dv/dr is assumed $10 \text{ km s}^{-1} \text{pc}^{-1}$ (solid lines) and $5 \text{ km s}^{-1} \text{pc}^{-1}$ (dashed lines).

Appendix 4 H₂ column density derived from the ¹²CO (*J*=1–0) and C¹⁸O (*J*=1–0) emission

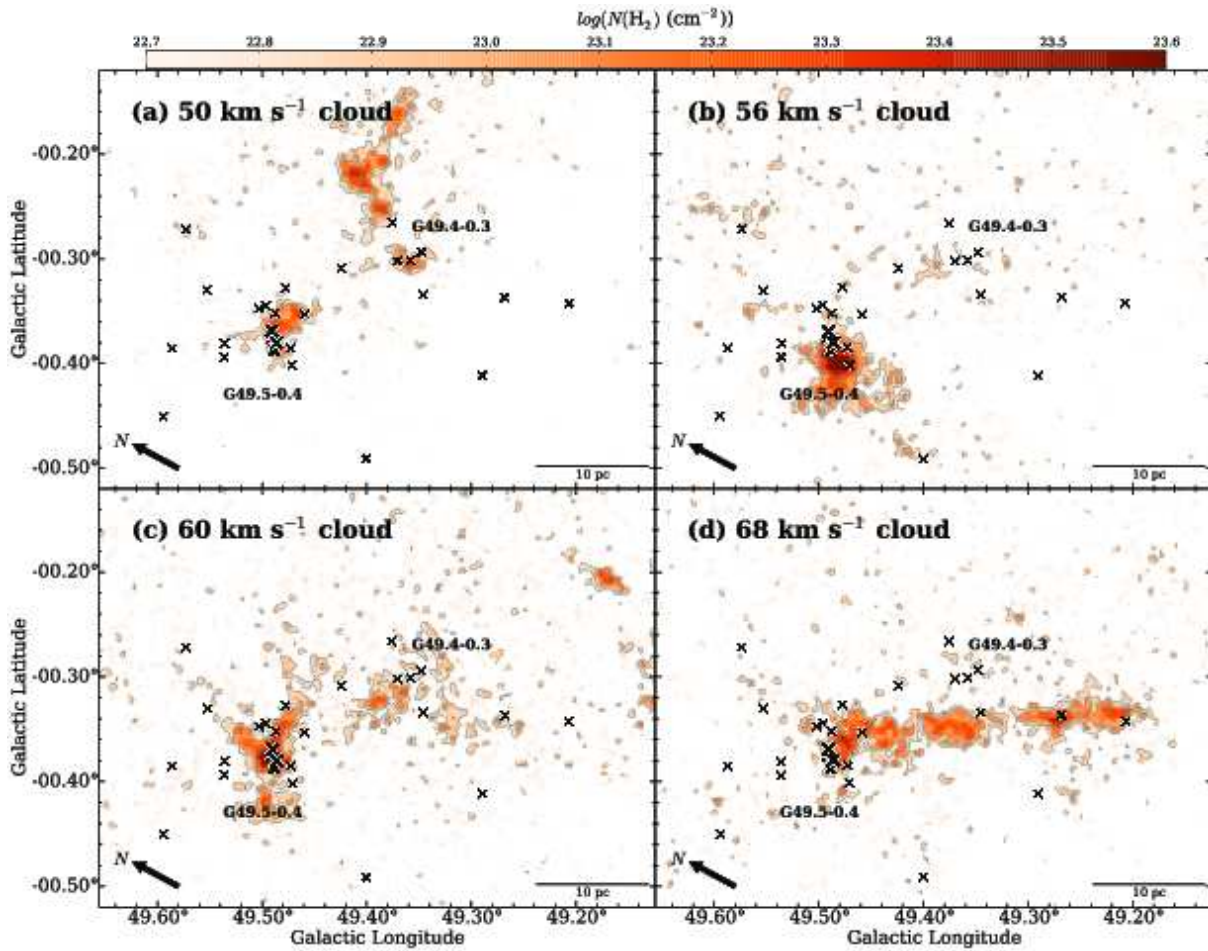


Fig. 22: The column density of H₂ molecules (derived from the ¹²CO (*J*=1–0) and C¹⁸O (*J*=1–0) emission) of the (a) 50, (b) 56, (c) 60, and (d) 68 km s⁻¹ clouds, with the integration ranges of 46.9–52.1, 52.8–58.6, 59.3–64.5, and 65.1–71.0 km s⁻¹, respectively. The gray contours are plotted with $6 \times 10^{22} \text{ cm}^{-2}$, $1 \times 10^{23} \text{ cm}^{-2}$, and $2 \times 10^{23} \text{ cm}^{-2}$ level. The crosses represent HII regions listed in Mehringer (1994).

Appendix 5 Fraction of the collision angle with random motion

Figure 23 shows normalized probability of collision angle θ ($0^\circ \leq \theta \leq 90^\circ$) and its cumulative fraction, when we assume that the motion of the colliding clouds are random. The normalized probability is relative to $\sin\theta$, and thus, its cumulative fraction is $1 - \cos\theta$.

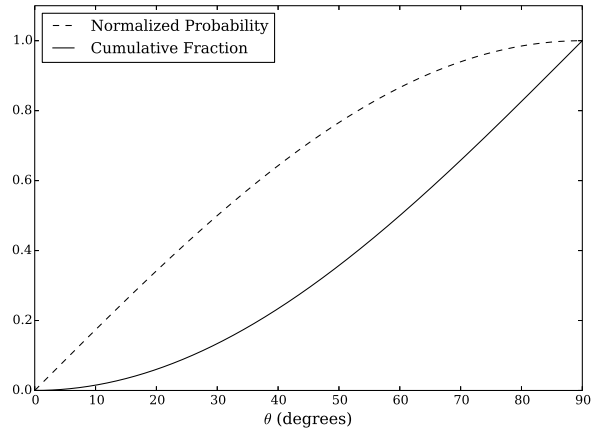


Fig. 23: The dashed curve and solid curve show normalized probability of collision angle θ ($0^\circ \leq \theta \leq 90^\circ$) and its cumulative fraction, respectively, when we assume that the motion of the colliding clouds are random. $\theta = 0^\circ$ means that the collision angle is parallel to the line of sight.